

Quantum Kernel Methods under Scrutiny: A Benchmarking Study

Jan Schnabel* and Marco Roth†

Fraunhofer Institute for Manufacturing Engineering and Automation IPA, Nobelstraße 12, D-70569 Stuttgart, Germany

(Dated: September 9, 2024)

Since the entry of kernel theory in the field of quantum machine learning, quantum kernel methods (QKMs) have gained increasing attention with regard to both probing promising applications and delivering intriguing research insights. Two common approaches for computing the underlying Gram matrix have emerged: fidelity quantum kernels (FQKs) and projected quantum kernels (PQKs). Benchmarking these methods is crucial to gain robust insights and to understand their practical utility. In this work, we present a comprehensive large-scale study examining QKMs based on FQKs and PQKs across a manifold of design choices. Our investigation encompasses both classification and regression tasks for five dataset families and 64 datasets, systematically comparing the use of FQKs and PQKs quantum support vector machines and kernel ridge regression. This resulted in over 20,000 models that were trained and optimized using a state-of-the-art hyperparameter search to ensure robust and comprehensive insights. We delve into the importance of hyperparameters on model performance scores and support our findings through rigorous correlation analyses. In this, we also closely inspect two data encoding strategies. Moreover, we provide an in-depth analysis addressing the design freedom of PQKs and explore the underlying principles responsible for learning. Our goal is not to identify the best-performing model for a specific task but to uncover the mechanisms that lead to effective QKMs and reveal universal patterns.

I. INTRODUCTION

Within the rapidly evolving field of quantum machine learning (QML) [1, 2], quantum kernel methods (QKMs) [3–9] have emerged as a particularly interesting and promising branch of research. For example, Liu *et al.* [10] have proven a rigorous quantum advantage for a classification task engineered from the discrete logarithm problem, although it requires a fault-tolerant quantum computer due to its reliance on a Shor-type data encoding. Beyond that, Refs. [3, 11] formally reveal that supervised QML models are kernel methods. In particular this implies that QKMs can be embedded into the rich mathematical framework of conventional kernel theory [12]. Among other appealing properties, this guarantees that when training a kernel-based model one finds the optimal solution due to the convexity of the training landscape.

The key idea of kernel methods are kernel functions that implicitly map input data into a higher-dimensional space where the learning problem becomes linear. Quantum kernel methods leverage the principles of quantum mechanics to perform these mappings into the exponentially large Hilbert space of quantum states. This is done using unitary operators, with input data encoded into rotation angles. In practice, this is realized by parameterized quantum circuits (PQCs) [3, 8, 13, 14], which in the context of quantum kernels are referred to as data encoding circuits. Two common approaches to evaluate the corresponding quantum kernel functions have become established: fidelity quantum kernels (FQKs) [3, 4, 7, 15] and projected quantum kernels (PQKs) [9, 16, 17]. A unified framework

for generalized trace-induced quantum kernels that includes FQKs and linear PQKs has been proposed recently in Ref. [9].

Wide-ranging application-oriented research in diverse domains emerged from the promising potentials of QKMs. This ranges from financial classification tasks [18] and quantum support vector machines (QSVM) for modeling transition probabilities in health and disability insurance [19] over a quantum kernel classifier for real high-dimensional data taken from the domain of cosmology [5] to QKMs for solving differential equations [20]. Apart from that, several works aim to understand the impact of certain properties of the underlying data encoding circuits on the model performance. In this regard, Hubregtsen *et al.* [21] performed a numerical study on the relation between classification accuracy and the PQC’s expressibility and entangling capability. Similar works [6, 22] explore the effect of entanglement in data encoding circuits on the performance of different classification tasks using FQKs. The importance of data preprocessing in FQKs is demonstrated in Ref. [23] based on experiments with real-world classification datasets. Moreover, there are recent efforts to automatize the encoding circuit architecture search, cf., e.g., Ref. [24] and references therein.

Equally, QKMs have been studied from a theoretical perspective. Kübler *et al.* [25] provide insights into the inductive bias of quantum kernels and conclude that quantum speed-ups may only occur if one manages to encode knowledge about the problem at hand into underlying quantum circuits, while encoding the same bias into a classical model would be hard. In this regard, Refs. [26, 27], the authors show that tuning the kernel’s bandwidth (which can be seen as a data preprocessing step) controls the model’s inductive bias. Consequently, these works identify the quantum kernel bandwidth as the key hyperparameter

* jan.schnabel@ipa.fraunhofer.de

† marco.roth@ipa.fraunhofer.de

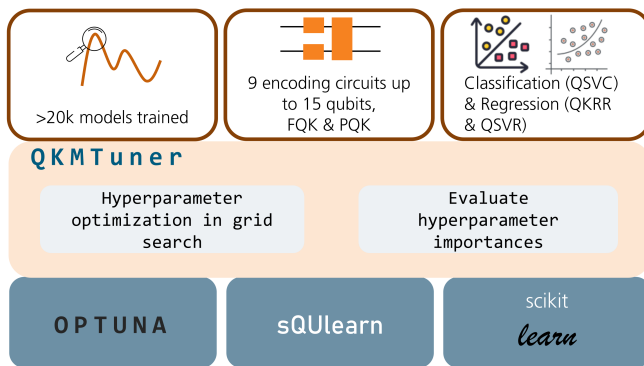


FIG. 1. Schematic illustration of the scope of this work and the basic functional principle of our software tool **QKMTuner** [30] used for the hyperparameter search of QKMs. We thoroughly investigate classification and regression tasks of five different dataset families and 64 datasets using QSVC as well as QSVR and QKRR, respectively leveraging both FQK and PQK approaches for evaluating the corresponding quantum kernel matrix. Corresponding data are embedded using nine data encoding circuits from the literature with up to 15 qubits. The code is based on the QML library sQUlearn [31], the (classical) hyperparameter optimization framework optuna [32] and the (classical) machine learning library scikit-learn [33].

controlling the expressiveness of the model and give a theory, which shows that varying the bandwidth enables generalization. However, the exponential size of the quantum feature space can hinder generalization and cause exponentially concentrated quantum kernel values [17, 28]. To circumvent this setback, Huang *et al.* [16] introduced the family of PQKs.¹ Their key findings include proving that classical learners can approximate quantum outputs with enough data and introducing methods for assessing potential quantum advantages. An illustrative application of these concepts is given in Ref. [29], where the authors provide numerical evidence against quantum advantage for FQKs on classical data. They show that tuning the kernel’s bandwidth improve the model performance and thus enables generalization, but also results in classically tractable kernels due to unfavorable geometric difference values.

Despite the variety of previous work, a comprehensive understanding of the wealth of design choices and their underlying mechanisms for various datasets is still incomplete. Our work attempts to make a contribution to closing this gap further by systematically analyzing the diversity of design criteria on a large scale and systematically examining both FQK and PQK approaches. We address this through state-of-the-art hyperparameter

search and correlation analysis. A schematic view on the scope of this work is shown in Fig. 1.

In this work, we conduct an extensive benchmarking study for classification and regression tasks using various QKMs such as quantum support vector classification (QSVC), quantum kernel ridge regression (QKRR), and quantum support vector regression (QSVR). Additionally, we generate a broad and general database by exploring nine popular data encoding circuits from the literature, offering a diverse analysis on the impact of the choice of encoding circuit. Beyond that, we propose two different encoding strategies to introduce feature redundancies and systematically compare them. Furthermore, the present work delves deep into the different design aspects of PQKs by examining the effects of measurement operators and outer kernels on model performance. We additionally address the question of which components of the PQK definition are responsible for learning, i.e., the projected quantum circuits versus the outer kernel. Finally, we numerically support all findings by rigorous correlation analysis. In total, this study resulted in over 20,000 quantum kernel models that were trained to provide an extensive database and to ensure robust and comprehensive insights. To facilitate this, we developed a software tool. Its basic functionality is shown in Fig. 1.

Previous studies have focused mostly on classification tasks. For example, Bowles *et al.* [34] conducted a large-scale evaluation of popular QML models, including Quantum Neural Networks (QNNs), FQKs and PQKs across various datasets. While QKMs were part of the study, the influence of the different design choices was not a particular focus. Their work was preceded by first attempts to systematically explore certain aspects of quantum model design, cf., e.g., Refs [35, 36]. Egginger *et al.* [37] have conducted a hyperparameter study for QKMs which extends the findings of Ref. [29] for PQKs. However, unlike this work, they exclusively focus on a single feature map (Hamiltonian evolution). In contrast to these previous findings, the present study offers an in-depth analysis of QKMs that significantly broadens the scope of investigation in multiple aspects and aims to answer aspects that have been previously untouched. This includes addressing regression problems, encoding mechanisms and a detailed analysis of PQKs. By extending previous findings we aim to contribute to a holistic understanding of QKMs.

This work is organized as follows. Section II introduces the theoretical basics of QKMs. Hereafter, we give detailed insights about the study design, including an overview on the multitude of different quantum kernel models considered in this work, an introduction of the datasets as well as implementation details for the corresponding hyperparameter optimization pipeline and the final experimental setup. In Sec. IV we first thoroughly investigate hyperparameter importances and model performances for classification and regression tasks across all datasets, encoding circuits and quantum kernel models and support corresponding findings with correlation analyses. Secondly,

¹ We note that Ref. [28] also derives exponential concentration bounds for PQKs. However, in practice PQKs usually suffer less from exponentially large Hilbert spaces, provided certain assumption on corresponding data encoding circuits are taken into account [17].

we carefully examine different data encoding strategies and give an in-depth analysis on different design options within the PQK approach, i.e., choice of outer kernel function and measurement operator. We discuss universal findings and patterns across all experiments and comment on the necessity of entanglement in data encoding circuits in Sec. V.

II. THEORETICAL BACKGROUND

One of the most interesting aspects of QKMs is that they can be formally embedded into the rich and powerful mathematical framework of classical kernel theory [3, 11]. The key idea behind the conventional kernelized approach to (supervised) machine learning is to find and analyze patterns by transforming the respective learning problem from the original input data domain \mathcal{X} to a higher-dimensional (potentially infinite-dimensional) *feature space* \mathcal{F} , where the learning tasks attains a trivial form, i.e., becomes a linear model. This mapping is accomplished by a *feature map* $\phi : \mathcal{X} \rightarrow \mathcal{F}; \mathbf{x} \mapsto \phi(\mathbf{x})$. Kernels, are real- or complex-valued symmetric and positive semi-definite functions of two input data points, $k : \mathcal{X} \times \mathcal{X} \rightarrow \mathbb{K}$, where \mathbb{K} can be \mathbb{R} or \mathbb{C} , respectively. In this regard, another central concept is that of *reproducing kernel Hilbert space* (RKHS) \mathcal{H}_k , which is an alternative feature spaces of a kernel; more precisely a feature space of functions constructed from the kernel. The RKHS uniquely determines the kernel and vice versa [38] and in addition, for every kernel there exists at least one feature map such that [11]

$$k(\mathbf{x}, \mathbf{x}') = \langle \phi(\mathbf{x}), \phi(\mathbf{x}') \rangle_{\mathcal{F}}. \quad (1)$$

Moreover, every feature map gives rise to a kernel. Less formally one can think of the RKHS as a space whose elementary functions, the kernels, assign a similarity measure between two data points \mathbf{x} and \mathbf{x}' .

A key result in kernel theory is the *representer theorem* [12, 39], which states that the function h that minimizes a regularized empirical risk loss, can always be represented as a finite (length of the training sample N) weighted linear combination of the kernel between some $\mathbf{x} \in \mathcal{X}$ and the training data \mathbf{x}_i , i.e.,

$$h(\mathbf{x}) = \sum_{i=1}^N c_i k(\mathbf{x}, \mathbf{x}_i). \quad (2)$$

Note that the number of terms in the sum is independent of the dimension of \mathcal{H}_k . The determination of the coefficients $\{c_i\}$ is a convex optimization problem [40]. This result is central to kernel methods used for supervised learning problems, e.g., SVMs [12], Gaussian Processes [41] or KRR [42]. All these algorithms are based on the kernel *Gram matrix* $G_{ij} = [k(\mathbf{x}_i, \mathbf{x}_j)]$.

In QML we process input data by encoding (embedding)

them into quantum states of the form

$$|\psi_{\theta}(\mathbf{x})\rangle = U(\mathbf{x}, \theta) |0\rangle^{\otimes n}, \quad (3)$$

where θ are variationally trainable parameters to refine the embedding into the quantum Hilbert space \mathcal{H}^Q . In practice, the unitary encoding operator $U(\mathbf{x}, \theta)$ can be implemented by a data encoding quantum circuit which manipulates an initial n -qubit quantum state $|0\rangle^{\otimes n}$. This reveals the striking similarity to kernel methods: Both utilize mathematical frameworks that map information into high-dimensional spaces for processing. In particular, as shown in Refs. [3, 11], the central concept of QKMs is that they can be formulated as a classical kernel method (e.g. SVM or KRR) whose kernel is computed using a quantum computer. Since quantum computations inherently feature the quantum mechanical principles of superposition and entanglement, the resulting quantum kernels hold the prospect of designing machine learning models that are able to learn complex problems that are out of reach for conventional machine learning methods [10].

In quantum computing, access to the Hilbert space of quantum states \mathcal{H}^Q is given by measurements, which, in analogy to conventional kernel theory, can be expressed by inner products of quantum states. This is schematically shown in Fig. 2. To formalize this, we define the density matrix $\rho_{\theta}(\mathbf{x}) = |\psi(\mathbf{x}, \theta)\rangle\langle\psi(\mathbf{x}, \theta)|$ as the corresponding data-encoding feature map [4, 11]. With this, we can leverage the native geometry of the quantum state space to defining a quantum kernel in a natural way using the Hilbert-Schmidt inner product, i.e.,

$$k_{\theta}^{\text{FQK}}(\mathbf{x}, \mathbf{x}') = \text{tr}[\rho_{\theta}(\mathbf{x})\rho_{\theta}(\mathbf{x}')] . \quad (4)$$

For pure states this definition reduces to

$$k_{\theta}^{\text{FQK}}(\mathbf{x}, \mathbf{x}') = |\langle\psi_{\theta}(\mathbf{x})|\psi_{\theta}(\mathbf{x}')\rangle|^2, \quad (5)$$

which, since it represents a fidelity-type metric, is referred to as the *fidelity quantum kernel* (FQK) [16]. Computing the full Gram matrix according to Eq. (5), in practice requires to execute two circuits and to sample the expectation value of the projector $P_0 = |0\rangle^{\otimes n}\langle 0|^{\otimes n}$, of a n -qubit system [8].

Recent work [16, 28, 29] demonstrates that with increasing problem size, FQKs can potentially suffer from *exponential concentration* leading to quantum models that may become untrainable. To alleviate this problem, Ref. [16] introduced the family of PQKs which project the quantum states to an approximate classical representation by using, e.g., reduced physical observables. As such, PQKs can be thought of defining features in a classical vector space by taking a detour through a quantum Hilbert space. The result is typically hard to compute due to the quantum detour but still retains desirable properties of the classical feature space. They thus have several appealing properties such as a linear scaling in terms of the needed quantum computing resources compared to FQKs.

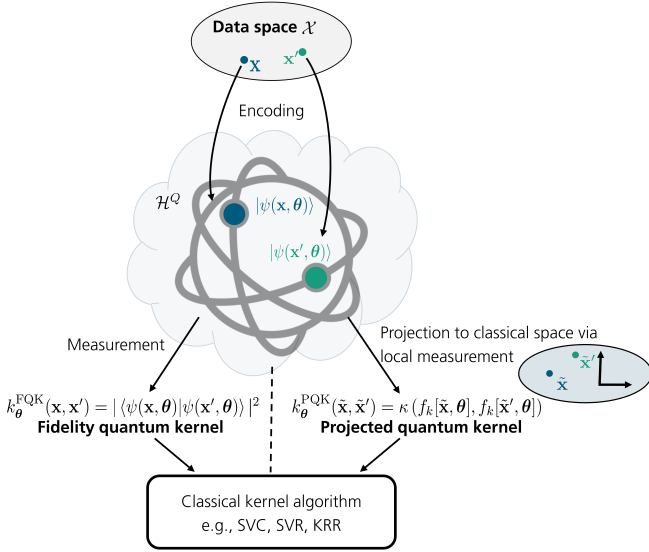


FIG. 2. Schematic illustration of the basic working principle of QKMs and its two most common approaches to compute respective quantum kernel Gram matrices. Data points are mapped from the input space \mathcal{X} to the quantum Hilbert space \mathcal{H}^Q by encoding them into quantum states $|\psi(\mathbf{x}, \boldsymbol{\theta})\rangle$. Access to \mathcal{H}^Q is provided by measurements, which can be expressed by inner products of quantum states in full analogy to classical kernel theory. **Left:** By using the native geometry of the quantum state space, i.e., the Hilbert-Schmidt inner product and leveraging this fidelity-type metric to define quantum kernels leads to FQKs, cf. Eq. (4). **Right:** Instead of directly processing quantum states within the quantum Hilbert space it has been shown that it can be beneficial to first project them to an approximate classical representation using, e.g., reduced physical observables. This concept gives rise to the family of PQKs. One of the simplest forms of defining PQKs is given in Eq. (8) and corresponds to measuring k -particle reduced density matrices and process the result with a classical kernel function κ . In both cases (FQK and PQK) the resulting kernel Gram matrices are subsequently passed to a classical kernel algorithm.

A simple way of defining PQKs is based on measuring k -particle reduced density matrices (k -RDMs),

$$\rho_{\boldsymbol{\theta}}^K(\mathbf{x}) = \text{tr}_{j \notin K} [\rho_{\boldsymbol{\theta}}(\mathbf{x})], \quad (6)$$

where K is the subset of k qubits from n , with $k \leq n$, and $\text{tr}_{j \notin K}$ is the partial trace over all qubits not in subset K . The projected quantum circuit results for \mathbf{x} and \mathbf{x}' are then used as features in some conventional outer kernel κ (e.g., RBF, Matérn, etc.). Measuring k -RDMs with respect to some observable O , corresponds to evaluating

$$\begin{aligned} f_k(\mathbf{x}, \boldsymbol{\theta}) &= \text{tr}(\rho_{\boldsymbol{\theta}}^K(\mathbf{x})O), \\ &= \text{tr}(\rho_{\boldsymbol{\theta}}(\mathbf{x})O^k), \end{aligned} \quad (7)$$

where O^k represents a k -local measurement operator acting on $k \leq n$ qubits, e.g. $P^{\otimes k} \otimes \mathbf{1}^{\otimes(n-k)}$, with P a Pauli operator. As such, PQKs can be generally defined as

$$k_{\boldsymbol{\theta}}^{\text{PQK}}(\mathbf{x}, \mathbf{x}') = \kappa(f_k[\mathbf{x}, \boldsymbol{\theta}], f_k[\mathbf{x}', \boldsymbol{\theta}]). \quad (8)$$

The most common PQK definition is based on measuring the 1-RDM on all qubits with respect to all Pauli operators $P \in \{X, Y, Z\}$, i.e. [16]

$$\begin{aligned} k_{\boldsymbol{\theta}}^{\text{PQK}}(\mathbf{x}, \mathbf{x}') &= \exp\left(-\gamma \sum_{k,P} [\text{tr}\{P\rho_{\boldsymbol{\theta}}^k(\mathbf{x})\} - \text{tr}\{P\rho_{\boldsymbol{\theta}}^k(\mathbf{x}')\}]^2\right) \\ &= \exp[-\gamma F_{\boldsymbol{\theta}}(\mathbf{x}, \mathbf{x}')], \end{aligned} \quad (9)$$

where $\gamma \in \mathbb{R}_+$ is a hyperparameter and $\rho_{\boldsymbol{\theta}}^k(\mathbf{x})$ is the 1-RDM, i.e., the partial trace of the quantum state $\rho_{\boldsymbol{\theta}}(\mathbf{x})$ over all qubits except for the k -th qubit; cf. Eq. (6). Here, we introduced the latter notation for later use in Sec. IV D. Note that unless otherwise stated, we are referring to the form as given in Eq. (9) when considering PQKs.

III. STUDY DESIGN

In this study, we systematically investigate the interplay of various hyperparameters in QKMs with the aim to identify patterns and mechanisms that enhance model performance (see Fig. 1). The following section details the methodological aspects of our study design, explaining the models and datasets we consider as well as providing insight into the implementation to realize this comprehensive analysis.

A. Models

The amount and range of hyperparameters that are inherently present in quantum kernel models generate a plethora of design choices. The most important hyperparameters are:

- *Number of qubits* n_{qubits} of the underlying encoding circuit used to encode the features of the dataset
- *Number of layers* n_{layers} of the corresponding encoding circuit
- The feature range $[f_{\min}, f_{\max}]$ used for scaling the dataset's features to respect the gate periodicity of the embedding and thus to prevent information loss. To obtain a single hyperparameter, we define the *width of embedding* in later analyses:

$$w_e = f_{\max} - f_{\min} \quad (10)$$

- *k -local measurement operator* O^k used for measuring k -RDMs as given in Eq. (7), which are subsequently used to define PQKs according to Eq. (8)
- *Regularization parameters*, these are the Tikhonov regularization strengths λ and C for QKRR and QSVR/QSVC, respectively. Additionally, for QSVR there is an additional hyperparameter ε , which specifies the range within which no penalty is associated in the training loss function with a point predicted within a distance ε from the actual value

- The functional form of the selected *outer kernel* κ in an PQK approach and therein the corresponding *length scale parameter(s)*, e.g., γ in case of a Gaussian (RBF) kernel.

We point out that data encoding unitaries (cf. Eq. (3)) additionally have multiple degrees of freedom. Data encoding circuits are at the heart of each QML method and significantly influence core properties of the resulting model. Generating problem-specific encoding circuits with, e.g., proper gate sets and corresponding structure marks a distinct research branch, cf., e.g., Refs. [24, 43]. This is beyond the scope of this work, wherefore we restrict ourselves to nine data encoding circuits from the QML literature [5, 7, 27, 28, 31, 44–46]. In this context, we randomly initialize the variationally trainable parameters of the encoding circuits that involve θ (cf. Eq. (3)) using a fixed seed. For details on these encoding circuit as well as corresponding illustrations, we refer to Appendix B.

B. Datasets

Selecting meaningful datasets for the sake of a conclusive study constitutes a highly nontrivial task. Therefore, our choice is mainly driven by aiming for datasets that are not too easy and whose complexity is ideally adjustable. Additionally, the size and dimensionality needs to be suited for QML applications with reasonable simulation time. Unless stated otherwise we used $M = 240$ training- and $M' = 60$ test data points within each dataset.

For studying classification, we use two binary classification datasets² introduced in Refs. [47, 48]. These datasets have been also used a previous benchmarking study [34].

two curves diff: This dataset describes the curvature and distance of two one-dimensional curves embedded into a d -dimensional space. We follow the data generation procedure of Ref. [34] and use low-degree (D) Fourier series to embed two sets of data sampled from a 1-d interval as curves into d dimensions while adding Gaussian noise $\sigma = 0.01$. The respective complexity can be controlled by fixing $d = 4$ and vary $D = 2, \dots, 20$, while adapting the offset $\Delta = 1/2D$.

hidden manifold diff: This dataset is created by generating inputs on a low-dimensional manifold and label them by a simple neural network initialized at random. The inputs are then projected to a final d -dimensional space. We use the dataset generation procedure as described in Ref. [34] and vary the dimensionality m of the manifold between $m = 2, \dots, 20$ but keep the feature dimension constant at $d = 4$.

The degree D and the dimensionality m of two curves diff and hidden manifold diff, respectively can be seen as control parameters adjusting the dataset complexity. To

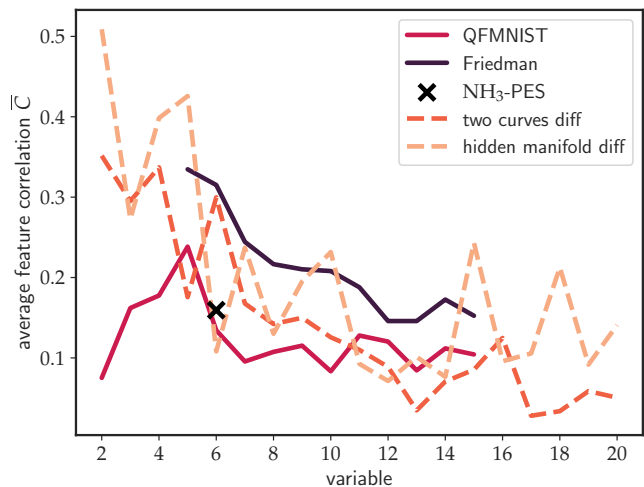


FIG. 3. Average feature correlations \bar{C} of the $[0, 1]$ -normalized features to the outputs to assess the dataset complexity for the datasets considered in this study. The classification datasets depend on variables between 2 and 20 that can be seen as controlling the difficulty, while for regression datasets this variable corresponds to the number of features. Note that higher values of this measure indicate simpler problems.

quantify this complexity, we use the average correlation \bar{C} of the respective $[0, 1]$ -normalized features to the output as suggested in Ref. [49] and as implemented in the ECoL package [49, 50].

The results are displayed in Fig. 3. Note that the dataset difficulty is inverse to the \bar{C} values, i.e., the lower means more difficult.

For regression, we select the following datasets:

Friedman #1: The Friedman #1 regression problem is described in Refs. [51, 52]. The dataset consists of $d \geq 5$ independent features distributed uniformly on the interval $[0, 1]$. The labels y satisfy

$$y(\mathbf{x}) = 10 \sin(\pi x_1 x_2) + 20(x_3 - 0.5)^2 + 10x_4 + 5x_5 + \sigma \mathcal{N}(0, 1), \quad (11)$$

where x_i with $i \in \{1, 2, 3, 4, 5\}$ is the i -th component of the data point \mathbf{x} and σ is the standard deviation of Gaussian noise applied to the output. We set $\sigma = 0.01$ for all simulations. Only $n = 5$ features contribute to the computation of the labels, while the remaining features are independent. Due to its non-linearity as well as its interaction between features and noise characteristics, this dataset mimics real-world regression scenarios. For this study, we generate datasets for $d = 5, \dots, 15$ features.

QFMNIST: This dataset is based on the fashion-MNIST dataset [53], which is sent through a quantum circuit to create a quantum-based dataset. We use the procedure as described in Ref. [8]. For this, first the fashion-MNIST feature dimension is reduced by principle component analysis. The resulting d features are then encoded into a quantum state using an n -qubit encoding circuit as pro-

² The resulting classification problems are balanced.

posed by Havlicek *et al.* [4]. The subsequent arbitrary single qubit rotations as applied in Ref. [8] are omitted. Finally, the labels for are generated by computing expectation values w.r.t. measuring the first qubit in the Pauli-Z basis. We generate datasets with $d = 2, \dots, 15$ principal components.

NH₃ Potential energy surface: This real world dataset provides taken from Ref. [54], which is a vast benchmark database for machine learning potential energy surfaces of a wide range of different molecules. Here, we use the ammonia data labeled with “STATIC-g32n1-1M” and “DZERO”. While the original dataset is in *xyz*-format we transformed them into internal coordinates (i.e. bond lengths and angles). Since nonlinear molecules with N atoms show $f = 3N - 6$ degrees of freedom, this dataset consists of six features with corresponding ground state energies (in Hartree) computed at CCSD(F12*)(T)/cc-pVDZ-F12 level of theory defining the labels. The dataset consists of 193 samples from which $M = 155$ are used for training and $M' = 38$ for testing.

For the Friedman#1 and QFMNIST regression problems the number of features can be viewed as control parameter to adjust the dataset complexity (cf. Fig. 3).

C. Experimental setup and Implementation

In the following we summarize the experimental setup for the hyperparameter search and provide some insights into the respective implementation.

All simulations in this study are based on sQUlearn with the PennyLane [55] statevector simulator device.

Design choices of quantum kernels We use sQUlearn for evaluating quantum kernel Gram matrices, which provides FQKs according to Eq. (5) and allows for defining PQKs as generally given in Eq. (8). For PQKs, we investigate the impact of different outer kernel functions κ . Specifically, we consider the Gaussian (RBF) kernel (cf., Eq. (9), which is the default in sQUlearn), the Matérn kernel [41] with $\nu = 1.5$, i.e.,

$$\kappa_{3/2}^{\text{Mat}}(\mathbf{x}, \mathbf{x}') = \left(1 + \frac{\sqrt{3}\|\mathbf{x} - \mathbf{x}'\|}{\ell}\right) \exp\left(-\frac{\sqrt{3}\|\mathbf{x} - \mathbf{x}'\|}{\ell}\right), \quad (12)$$

and the RationalQuadratic kernel [56], i.e.,

$$\kappa^{\text{RQ}}(\mathbf{x}, \mathbf{x}') = \left(1 + \frac{\|\mathbf{x} - \mathbf{x}'\|^2}{2\alpha\ell^2}\right)^{-\alpha}. \quad (13)$$

Moreover, we study the effect of using different k -local measurement operators for defining PQKs (cf., Eqs. (7) and (8)). We use the 1-RDM on all qubits w.r.t. different (combinations of) Pauli operators

$$O^{k=1} \in \{X_{k=1}, Z_{k=1}, (X_{k=1} + Z_{k=1}), \sum_{P \in \mathcal{P}} P_{k=1}\}, \quad (14)$$

where $\mathcal{P} = \{X, Y, Z\}$ is the set of Pauli operators (cf. Eq. (9)) and $P_{k=1}$ denotes all possible 1-qubit operators with Pauli operator P of a n -qubit system, i.e.,

$$P_{k=1} = \sum_{k=1}^n P^k, \quad (15)$$

where $P^k = \mathbb{1}_1 \otimes \dots \otimes P^k \otimes \mathbb{1}_{k+1} \otimes \dots \otimes \mathbb{1}_n$ is the Pauli operator P acting on the k -th qubit. Additionally, we consider measuring the 2-RDM on all qubit combinations w.r.t. different Pauli operator configurations

$$O^{k=2} \in \{X_{k=2}, Z_{k=2}, (X_{k=2} + Z_{k=2}), \sum_{P \in \mathcal{P}} P_{k=2}\}, \quad (16)$$

where $P_{k=2}$ generally represents all possible permutations $S_2(n)$ of 2-qubit Pauli measurements from n qubits, i.e.

$$P_{k=2} = \sum_{K \in S_2(n)} P^K, \quad (17)$$

with K the subset of 2 qubits from n . Finally, we also check for one PQK definition with a combination of 1-RDM and 2-RDM measurements

$$P^{1+2} = \sum_{P \in \mathcal{P}} (P_{k=1} + P_{k=2}). \quad (18)$$

Hyperparameters of quantum kernel methods The QKMs as implemented in sQUlearn work analogously to their classical counterparts in *scikit-learn*. In this work we use QKRR and QSVR for regression tasks and Q SVC for solving classification problems. The corresponding regularization hyperparameters are λ , C and ε as well as C , respectively.

QKMTuner for hyperparameter search We develop the tool QKMTuner to facilitate the extensive hyperparameter search of this study. The code is based on sQUlearn [31], optuna [32] and scikit-learn [33]. QKMTuner consists of two main routines: a hyperparameter optimization within a grid search and a method for studying hyperparameter importances; cf. Fig. 1. The grid-search is given a list of data encoding circuits for each of which it builds a user-defined $n_{\text{qubits}} \times n_{\text{layers}}$ -grid on which a hyperparameter search is performed for each grid point and each data encoding circuit for a given dataset. For evaluating hyperparameter importances, the respective method only takes a list of data encoding circuits and automatically searches for the optimal hyperparameters including n_{qubits} and n_{layers} . In both cases, the hyperparameters are determined by maximizing the minimum between the mean and median of five-fold cross-validation scores. This choice of the objective function prevents the scores from becoming too optimistic and thus helps to prevent overfitting towards an easy fold. The respective scoring method can be set manually, whereas in this work we use the area under the receiver operating characteristic curve (ROC-AUC) from prediction scores for classification and (negative) mean squared error (MSE) for regression

tasks, respectively. For hyperparameter sampling we use the tree-structured parzen estimator [57], albeit different algorithms as provided by optuna are supported. The code of QKMTuner is available in Ref. [30].

Data preprocessing We scale the dataset features to the range $[f_{\min}, f_{\max}]$ with $f_{\min} \in [-\frac{\pi}{2}, 0)$ and $f_{\max} \in (0, \frac{\pi}{2}]$ as in Ref. [34] and consider f_{\max} (f_{\min}), or equivalently $w_e = f_{\max} - f_{\min}$, cf. Eq. (10), as additional hyperparameters which are optimized within QKMTuner³. For all regression datasets we additionally scale the corresponding target values to $[0, 1]$. By using pipelines, we ensure that data scaling is part of the cross-validation step.

IV. RESULTS

In this section, we discuss all findings from the different types of experiments that have been performed, before we summarize these results in terms of identifying general patterns in Sec. V.

A. Hyperparameter Importances

The investigation of hyperparameter importances for optimizing a given objective function (in this work the five-fold cross-validation scores) helps in effective model tuning by highlighting critical hyperparameters. We determine the importance of hyperparameters using “fANOVA”—a random forest-based algorithm implemented through optuna [58]. Here, the sum of resulting importance values are normalized to one and higher values imply that the associated parameters are more important. For the regression datasets we analyze this for the NH₃-PES dataset and the Friedman and QFMNIST datasets with five features, respectively. For classification, we consider all datasets within the two curves diff and hidden manifold diff families, i.e., $D, m = 2, \dots, 20$. In both cases we investigate various model configurations in terms of encoding circuits and kernel type and QKM. Here, we always impose that n_{qubits} can only assume values that are integer multiples of the number of features of the respective dataset, with a maximum of $n_{\text{qubits}}^{\text{max}} = 15$.

Regression Tasks

The hyperparameter importances for the regression datasets, aggregated for each model across different encoding circuits, are shown in Fig. 4. By comparing the results from (a) to (c), we observe some similar trends. First, for

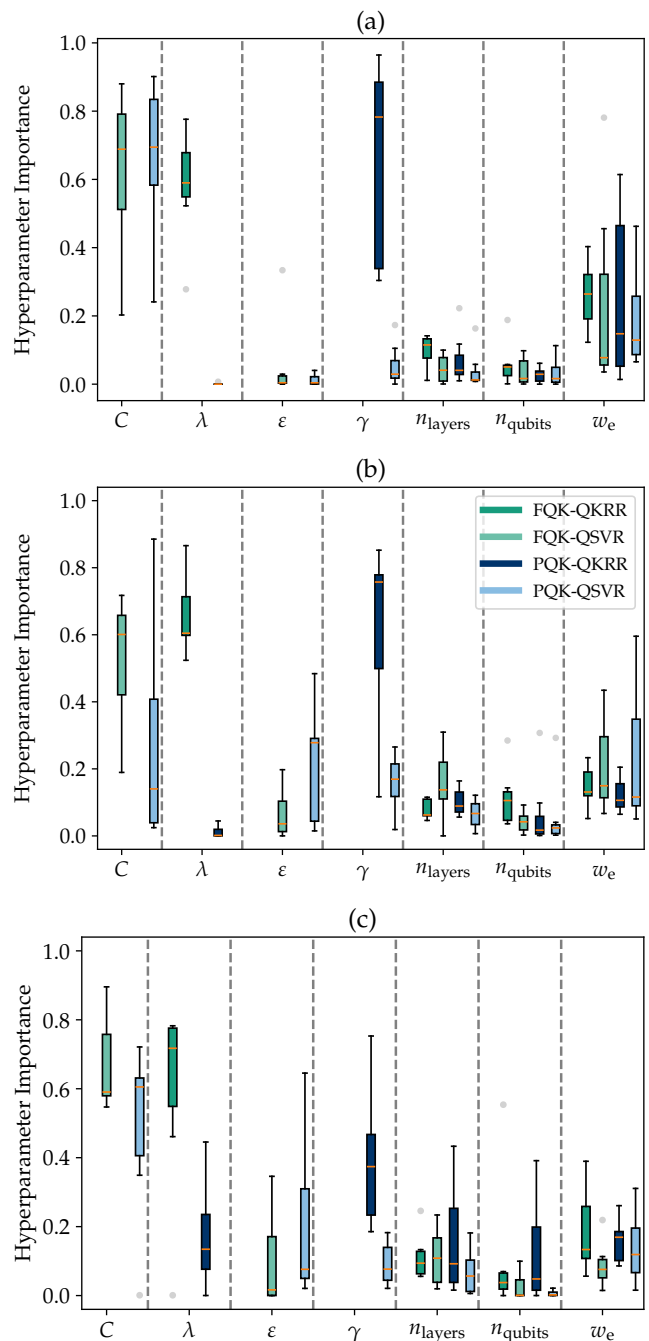


FIG. 4. Comparison of hyperparameter importances for optimizing the five-fold cross-validation score in the corresponding hyperparameter optimizations of the regression tasks. The **Friedman** dataset with $n = 5$ features is shown in (a), the **QFMNIST** results with $n = 5$ components are illustrated in (b), and the data corresponding to the **NH₃-PES** are given in (c). The results for each model and dataset are aggregated over different encoding circuits in each case. Here, we always impose that n_{qubits} can only be integer multiples of the number of features present in the respective dataset, with a maximum of $n_{\text{qubits}}^{\text{max}} = 15$.

³ This holds for all data encoding unitaries, except for the **ChebyshevPQC**, which encodes features non-linearly as $\arccos(x)$, wherefore we adapt $\tilde{f}_{\min} \in [-1.0, 0)$ and $\tilde{f}_{\max} \in (0, 1.0]$

FQK-QKRR and FQK-QSVR the Tikhonov regulariza-

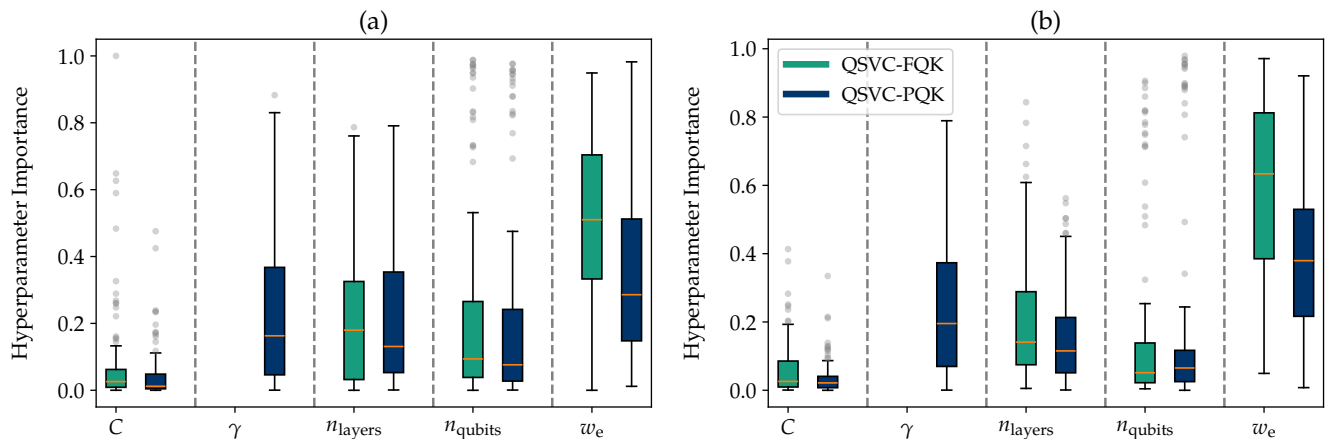


FIG. 5. Comparison of hyperparameter importances for optimizing the five-fold cross-validation score in the corresponding hyperparameter optimizations of the classification tasks of this study. For both QSVC-FQK and QSVC-PQK, the results are aggregated across all datasets within the correlating dataset family and all encoding circuits. The results corresponding to the **two curves diff** family are shown in (a). The **hidden manifold diff** dataset family is depicted in (b). In both cases we impose that n_{qubits} can only be integer multiples of the number of features ($d = 4$), with a maximum of $n_{\text{qubits}}^{\text{max}} = 15$.

tion λ and C , respectively appears to be most important to obtain sufficiently well trained quantum regressors. This is followed by the embedding width parameter w_e used for feature scaling, while n_{layers} and n_{qubits} of the encoding circuits are relatively unimportant. For FQK-QSVR, the ε parameter seems to be rather unimportant as well. Further, for PQK-QKRR the length scale parameter γ of the Gaussian outer kernel, cf. Eq. (9), is most important, again followed by the feature scaling parameter w_e . Once more, the number of qubits and layers are similarly unimportant, only λ is less important. Finally, in the case of PQK-QSVR, again the regularization parameter C appears to be most important (at least for the Friedman and NH_3 datasets), followed by ε for QFMNIST and NH_3 . The feature scaling w_e is similarly important across all datasets, while γ is roughly as important only in the case of QFMNIST and NH_3 , while it is least important for the Friedman dataset. The behavior of n_{qubits} and n_{layers} is then again comparable across all datasets.

Interestingly, the behaviour of some parameters within the QFMNIST and NH_3 datasets is more similar than that of the Friedman dataset. This might be due to their quantum nature. While the QFMNIST is an engineered dataset, the NH_3 dataset represents true quantum data as it results from solving the stationary electronic Schrödinger equation of the ammonia molecule. However, overall there are no significant differences between classical and quantum data considered in this study. Rather, it is remarkable that the number of qubits and layers still seems to play an almost negligible role in the training of a quantum regressor.

Finally, we note that the largest differences to other results occur for PQK-QSVR within QFMNIST. Here, the regularization C shows a vanishing median value and an increased importance of both ε and w_e with other param-

eters being similar important. In this case, the differences between hyperparameter importances on average seem to be reduced towards all parameters becoming equally important.

Classification Tasks

Figure 5 displays the hyperparameter importances for the two curves diff and hidden manifold diff dataset families. Here, for both FQK and PQK QKMs, we aggregated results across all corresponding data subsets and encoding circuits. The results in Figs. 5 (a) and (b) clearly reveal that w_e is most important in order to obtain sufficiently well trained quantum classifiers. This is in contrast to the regression results, where regularization or the γ parameter are more important. The importance of feature scaling can be directly related to the concept of kernel bandwidth tuning as reported, e.g., in Refs. [26, 27] and is in accordance with the results presented therein. Moreover, it perfectly agrees with the recent outcomes of Ref. [37], where the scaling parameter t of the Hamiltonian evolution feature map was evaluated as the most important parameter in PQKs for both the accuracy as well as for the geometric difference. In addition to that, we provide some evidence that the importance of feature prescaling is slightly more pronounced for FQKs than for PQKs. This, however, is not surprising, given the fact that the γ -parameter in PQKs of the form of Eq. (9) acts as an additional (classical) bandwidth tuning parameter. Here, γ is the second most important parameter for PQK models. The regularization parameter C of QSVC appears to be comparatively unimportant, except for some outliers. This is even more pronounced for PQKs than for FQKs. Compared to Fig. 4, the results in Fig. 5 clearly indicate that n_{qubits} and n_{layers} appears to be more important,

with tuning the number of layers being more important than potentially encoding features redundantly on the number of qubits. This could hint at the more difficult the dataset, which for $D, m \geq 6$ is the case for the classification datasets (cf. Fig. 3), the more important feature redundancies become and adjusting the number of layers accordingly.

B. Model Performance and Correlation Analysis

In the preceding section, we analyzed the impact of various QKM hyperparameters on effective model tuning, specifically exploring the optimization question of how to obtain an optimally trained model. In the following, we delve into the relationships concerning the generalizability of QKMs. Due to the insights from the hyperparameter importances in Fig. 4 and 5, we fix n_{qubits} for every dataset to the respective number of features for all upcoming investigations and perform hyperparameter optimizations for every data encoding circuit with $n_{\text{layers}} \in [1, 8]$.

First, we examine the test performance of different QKM models as a function of increasing dataset complexity. This analysis is given in Fig. 6, which illustrates the results for the Friedman, QFMNIST, two curves diff, and hidden manifold diff datasets. In these cases results for each QKM and dataset within the respective dataset family are aggregated across the data encoding circuits with corresponding obtained optimal n_{layers}^* , yielding the best MSE or ROC-AUC score, respectively.

A comparison with Fig. 3 indicates that the behavior of test performance scores as a function of a control parameter qualitatively aligns with the increasing complexity of the respective datasets. This confirms that \mathcal{C} is a useful measure of complexity. The comparison between FQK and PQK approaches in Figs. 6 (a) and (b), particularly for larger problem instances with increasing n , which transfers to increasing n_{qubits} , reveals no significant performance differences. While PQKs demonstrate slightly superior performance, the difference is not as substantial as one might anticipate given the challenges posed in connection with exponential concentration [28], whose regime we may already enter with up to 15 qubits. The absence of this observation may be explained by the presence of the bandwidth tuning parameter w_e , which shows significant correlations with performance scores as discussed below. The comparison between QKRR and QSVR each within FQK or PQK approaches does not reveal a clear advantage for either method. For the Friedman dataset we notice comparatively large interquartile ranges (IQRs) for QKRR/QSVR-PQK approaches towards datasets with lower dataset complexity, especially for $n = 6$. By inspecting the corresponding training scores in Fig. A10 (a) in Appendix D 1, we may attribute this trend to poorly trained models for QSVR-PQK, while for QKRR-PQK this may be due to overfitting. The latter could probably be alleviated by increasing the number of training data

which is beyond the scope of this work. Moreover, the QFMNIST($n = 2$) dataset constitutes the only case for which we observe a clear performance difference between FQK and PQK. Regarding the classification tasks, we do not realize any significant difference between both QKMs.

Beyond that, we generally observe many outliers exhibiting particularly poor test performance scores. The comparison with associated training performance scores in Fig. A10 shows that this may again result from overfitting for certain model combinations which might be too expressive for the respective dataset. This may also suggest that the design of data encoding circuits should follow a data-centric approach as, e.g., pioneered in Ref. [24]. Finally, we note that the propensity for overfitting is not only present for the two curves diff, as previously noted in Ref. [34], we also observe this for the Friedman and QFMNIST regression families. As shown in Appendix D 1 this is most dominant for QKRR-FQK/PQK approaches with increasing dataset complexity, while QSVR appears to be more robust. The hidden manifold diff dataset, on the other hand, is not as prone to overfitting. However, in total we point out here that our test size is quite small ($M' = 60$, as mentioned in Sec. III B) which represents a clear limitation towards more detailed statements in this direction. This should be carefully considered in future studies.

To investigate the impact of data encoding circuits on the performance we aggregate results across all datasets within each family and $n_{\text{layers}} \in [1, 8]$ and then re-plot the data, ordered by the encoding circuits. This is exemplified in Fig. 7 for the Friedman (regression) and the two curves diff dataset (classification). The results corresponding to the other dataset families of this study are shown in Fig. A11 in Appendix B. When examining the performance scores for a single dataset within a dataset family, significant performance differences emerge. This can be seen in Figs. 7 (a) and (c). Here, the ‘‘HZY_CZ_EncodingCircuit’’ performs particularly poor in regression tasks, while the ‘‘ChebyshevPQC encoding circuit’’ under performs in classification tasks, both for FQK and PQK approaches. However, when considering performance scores aggregated across all datasets within a dataset family, we observe that, except for the ‘‘ChebyshevPQC’’ in the QSVC-FQK case, all encoding circuits perform comparably, cf. Figs. 7 (b) and (d). No clear winner emerges, and in fact, each encoding circuit has upper whiskers indicating perfect test performance scores. The IQRs are also very similar across all encoding circuits. Furthermore, this aggregated analysis does not reveal any significant performance differences between FQK and PQK approaches. The similarity in the aggregated test performance scores is more pronounced in the classification problem illustrated (see Appendix D for analogous plots for other datasets). This again supports the argument for problem-specific data encoding architecture search [24, 43].

In earlier studies [34], it has been found that data encod-

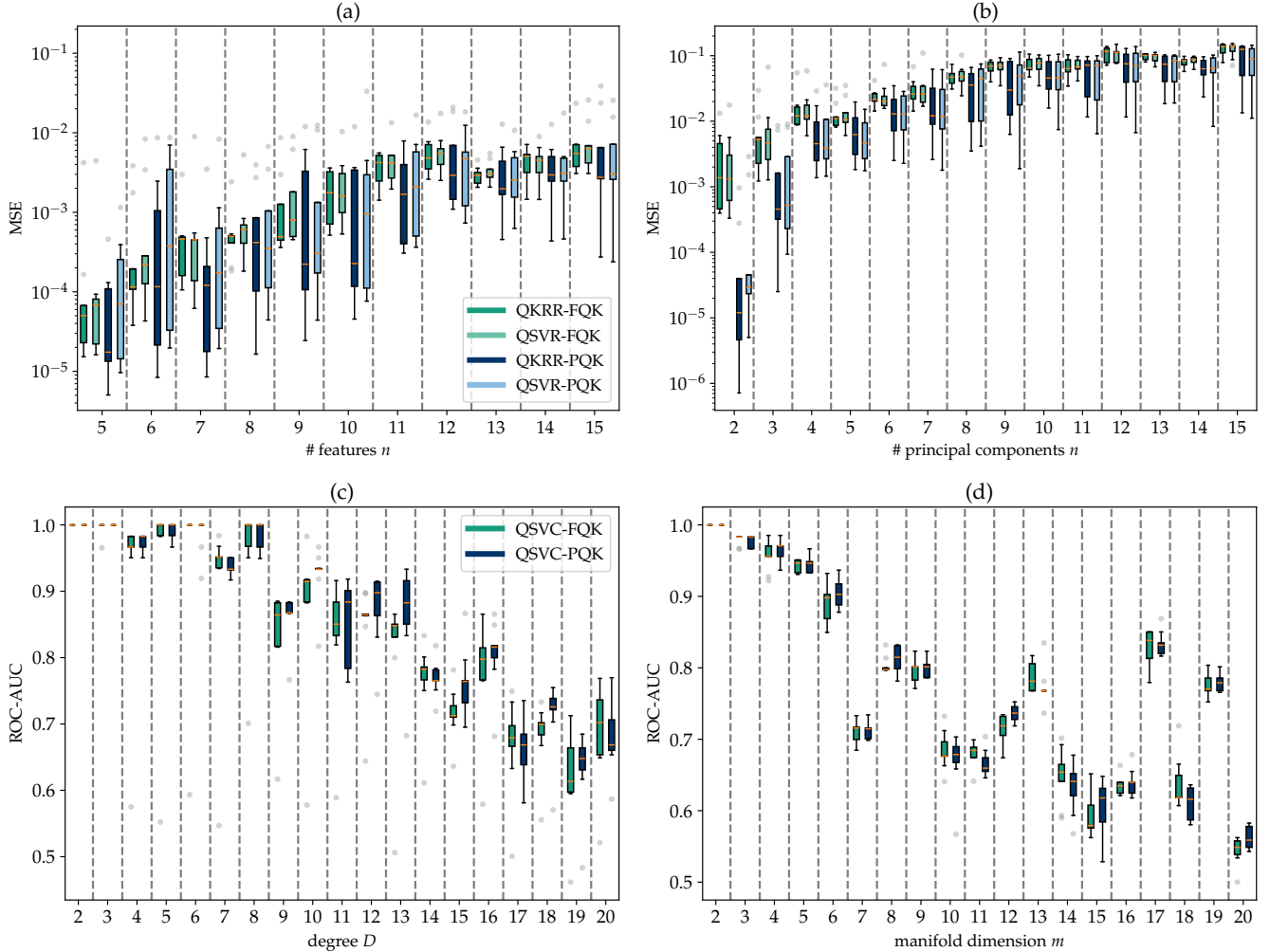


FIG. 6. Overview of test performance scores of respective QKMs as a function of increasing dataset complexity. Results within each dataset are aggregated across all data encoding circuits with corresponding optimal n_{layers}^* yielding minimum/maximum test performance scores for regression/classification, respectively. The **upper panel** displays two **regression** tasks, where the MSE is used to measure the prediction accuracy. The **Friedman** dataset family is shown in (a), where the number of features n can be viewed as control parameter for dataset complexity. The **QFMNIST** dataset family is shown in (b), where the number of principal components used in the dataset generation procedure controls the dataset complexity. The **lower panel** illustrates the two **classification** tasks of this study, where we use the ROC-AUC score to assess classification accuracy. In (c) we show the **two curves diff** dataset family with the degree D controlling the complexity. The **hidden manifold diff** family is given in (d) with the manifold dimension m as respective control parameter.

ing circuits without entanglement can perform surprisingly well. In our case, these are the “SeparableRx” and “ZFeatureMap” encoding circuits. As demonstrated in Ref. [27] for FQKs, the “SeparableRx” circuit is analytically tractable, and this can be straightforwardly extended to PQKs. Similarly, the “ZFeatureMap”, which incorporates additional Hadamard gates, also demonstrates comparable performance. This raises the possibility that driving forces other than “quantumness” might be fostering the performance of QKMs. This observation underscores the need for further comprehensive and systematic investigations into the underlying factors contributing to QKM performance.

To gain even deeper insights, Fig. 8 provides an exemplary overview on the results of the correlation analyses between QKM hyperparameters and test performance scores, as well as between the hyperparameters themselves for the QFMNIST dataset family. We refer to Fig. A12 in the Appendix D 1 for a summary of all other dataset families investigated in this study. The results are aggregated across datasets within a dataset family and across all considered encoding circuits and $n_{\text{layers}} \in [1, 8]$, respectively. Due to the presence of numerous outliers, cf. Figs. 6 and 7, we employ Spearman correlation analysis, which does not assume normally distributed variables or that the relationship between variables is linear. Fig-

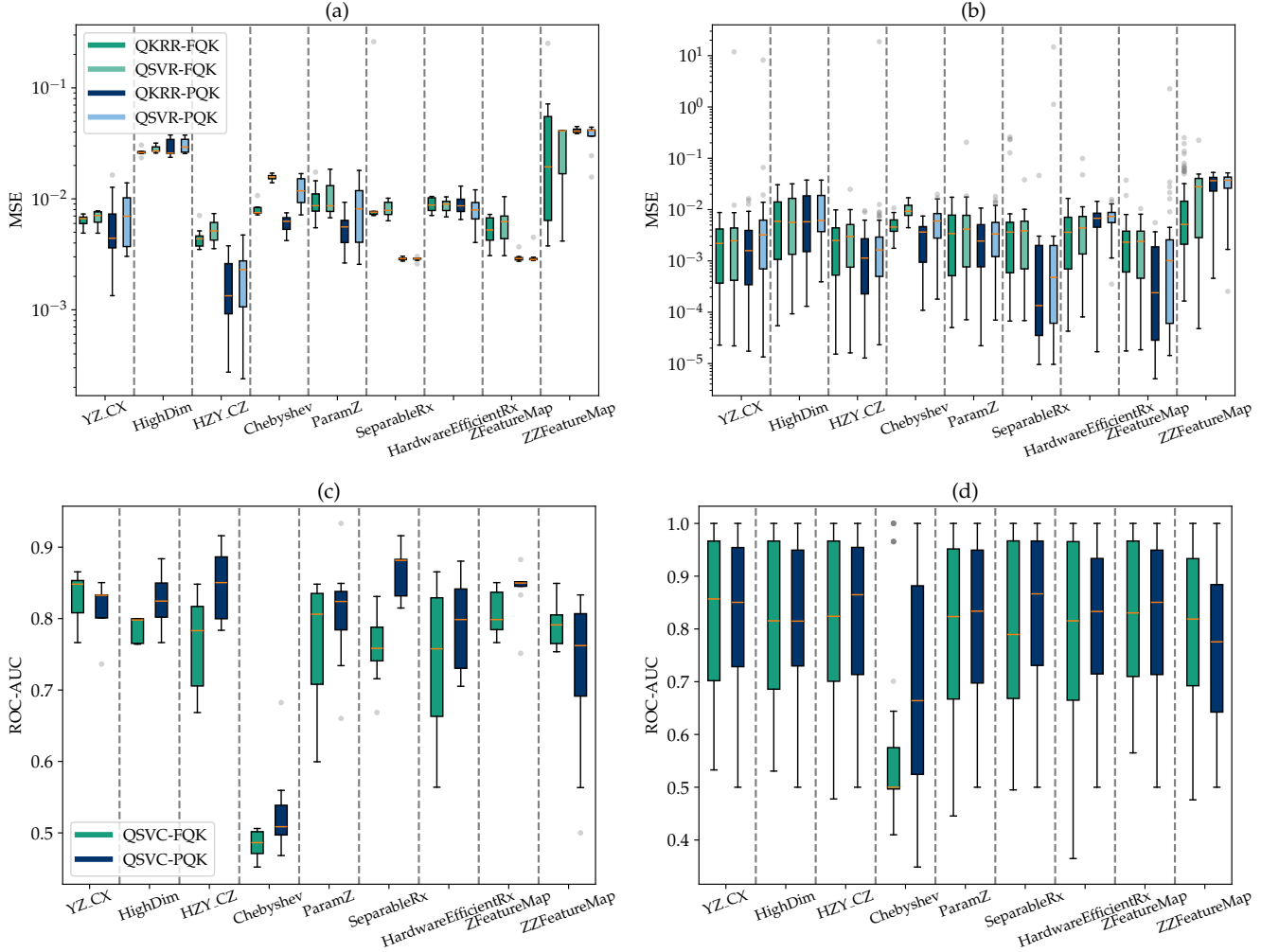


FIG. 7. Insight into the impact of data encoding circuits on test performance scores. Results are aggregated across all datasets within the respective family and $n_{\text{layers}} \in [1, 8]$. The **upper panel** exemplifies this for the **Friedman** regression problem. In (a) we show results corresponding to the dataset with $n = 15$ features. Here, test performance scores, as measured by MSE, are aggregated over $n_{\text{layers}} \in [1, 8]$ per regression method (QSVR/QKRR) and quantum kernel (FQK/PQK). The findings in (b) represent test performance scores aggregated over all datasets in the Friedman family. The **lower panel** details the **two curves diff** dataset. In (c), we display test performances, as measured by ROC-AUC score, aggregated over $n_{\text{layers}} \in [1, 8]$ for the dataset with degree $D = 13$. Aggregated results across all datasets are depicted in (d).

ure 8 indicates statistically significant correlations by green-highlighted p -values. Note that the signs of the correlation coefficients work in opposite directions for regression and classification tasks, due to the use of MSE and ROC-AUC metrics, respectively. In line with the findings from the analysis of hyperparameter importance in Figs. 4 and 5, we observe moderate to strong statistically significant correlations between test performance scores and the various regularization parameters, i.e., λ and C for QKRR and QSVR/QSVC, respectively as well as ε for QSVR. Additionally, consistent with findings on bandwidth tuning [26, 27], we frequently (also considering the findings from Fig. A12) observe moderate and statistically significant correlations between the feature scaling parameter w_e , cf. Eq. (10), and performance scores.

This parameter often also correlates with the n_{layers} . For QSVR-/QSVC-PQK models, moderate correlations are also observed between the length-scale parameter γ of the Gaussian outer kernel and test performance. With the complete correlation analyses in mind, cf. Fig. A12, only in the case of the artificial quantum dataset QFMNIST, we observe very weak correlations between n_{layers} and the test MSE.

Given these insights, we may acquire an improved understanding of the poor performance regimes observed in Figs. 6 and 7 if we interpret the strong correlations between regularization parameters and model performance as indicative of ill-conditioned training kernel Gram matrices. This could be a result of unfavorable embeddings of the underlying data into the quantum Hilbert space.

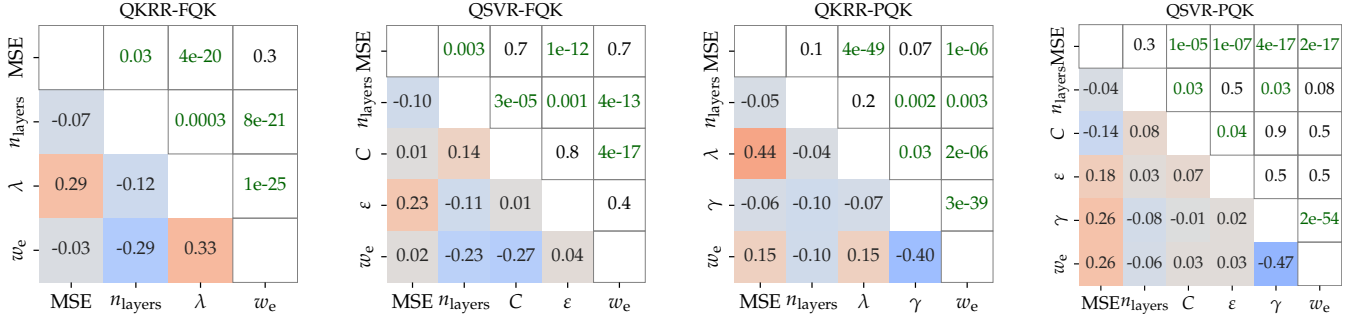


FIG. 8. Overview of the Spearman correlation analyses between QKM hyperparameters and test performance scores, as well as between the hyperparameters themselves, for the QFMNIST dataset family. The results correspond to aggregating data across all datasets, encoding circuits, and $n_{\text{layers}} \in [1, 8]$. The Spearman correlation coefficients are given on the lower triangles of the respective matrices (with blue for negative to red for positive coefficients), while the upper triangles display corresponding p -values. Here, statistically significant correlations ($p \leq 0.05$) are highlighted in green. Since we use the MSE to evaluate regression performance and the ROC-AUC score in case of classification, respectively, we note that the signs of associated correlation coefficients work in opposite direction; i.e., e.g., negative correlation with MSE means better regression performance, while it is the other way round for classification.

Combined with the obtained correlations between performance scores and w_e as well as γ , this could further challenge our understanding of “quantumness” of QKMs, apart from the already mentioned entanglement problem.

C. Data Encoding Strategies

It is known [11, 14] that the number of qubits and layers of data encoding circuits determine the Fourier frequency spectrum of the resulting quantum model and that encoding features redundantly can help in getting more accurate results. However, there are some degrees of freedom how to do this exactly. Therefore, we try shed some light on this in the context of QKMs. To this end, we study quantum kernel models built from encoding circuits according to the two data embedding schemes illustrated in Fig. 9. In both embedding schemes, features are encoded in the qubits from top to bottom. Differences in the two encoding strategies occur when the number of qubits is larger than the number of features. In “option 1”, after all features have been encoded once in a layer, the encoding is repeated and then cut off once the final qubit is reached. In “option 2”, the features enumeration of features is not reset at the next layer. As a consequence, each feature in “option 1” is always assigned to the same qubit, whereas in “option 2” the features can be shuffled across qubits.

In the case of the regression (QKRR and QSVR), Fig. (10) shows exemplary the result for the QFMNIST dataset for $n = 5$. The results for each quantum kernel were aggregated across the regression methods and the respective encoding circuits. Then, the median of the resulting MSE test score was calculated. For FQK, both embedding options show that largest scores are achieved for ten qubits, i.e., for integer multiples of the number of features. It can be seen that higher scores occur more frequently

with embedding “option 2”. For PQK, it appears that no feature redundancies are necessary in either case. Here, however, embedding “option 1” often delivers larger scores.

Figure 11 displays the results for the two curves diff classification dataset for $D = 13$ (the number of features is still fixed to $d = 4$). The results were aggregated over the respective encoding circuits and then the median of the ROC-AUC test scores was evaluated. It can be seen that here, unlike in the case of regression, both embedding options for both quantum kernels (FQK and PQK) deliver the best classification accuracies for non-integer multiples

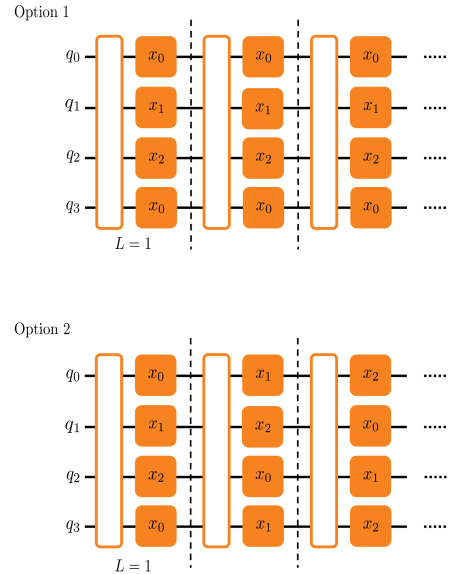


FIG. 9. Schematic illustration of two different data encoding options considered in the investigations of Sec. IV C.

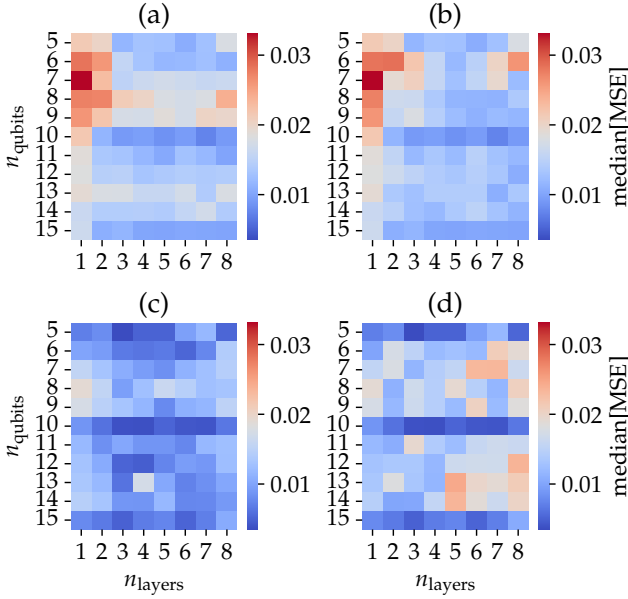


FIG. 10. Investigation of different encoding strategies as illustrated in Fig. 9 for FQK and PQK approaches for the QFMNIST regression dataset with $n = 5$ principal components. The results were aggregated over QKRR and QSVR approaches as well as over the corresponding encoding circuits, and then the median of the MSE test scores was calculated in each case. The upper panel corresponds to FQKs, while the lower panel shows PQKs, whereas the left column represents “option 1” and the right column “option 2”, respectively. As such, we have: (a) FQK, option 1, (b) FQK, option 2, (c) PQK, option 1 and (d) PQK, option 2.

of the number of features. Here, “option 1” performs better in each case. In addition, there seems to be a tendency for the larger n_{layers} and the larger n_{qubits} the better the classification accuracy. This result might be due to the much greater dataset complexity the two curves diff ($D = 13$) dataset compared to QFMNIST with $n = 5$.

However, the findings discussed here also apply to the remaining regression and classification datasets in this study. These are summarized in detail in Appendix D 2 in Figs. A13, A14 and A15.

D. In-depth Analysis of PQK Design Options

Beyond tuning various hyperparameters and selecting appropriate data encoding strategies, QKMs based on PQKs according to Eq. (8) have additional degrees of freedom in model design. Specifically, any outer kernel function κ that satisfies the requirements of a kernel function can be applied to the features computed by quantum inputs according to Eq. (7). Here, the exact form of the measurement operator O^k used to define the projected quantum circuits is not fixed either. To

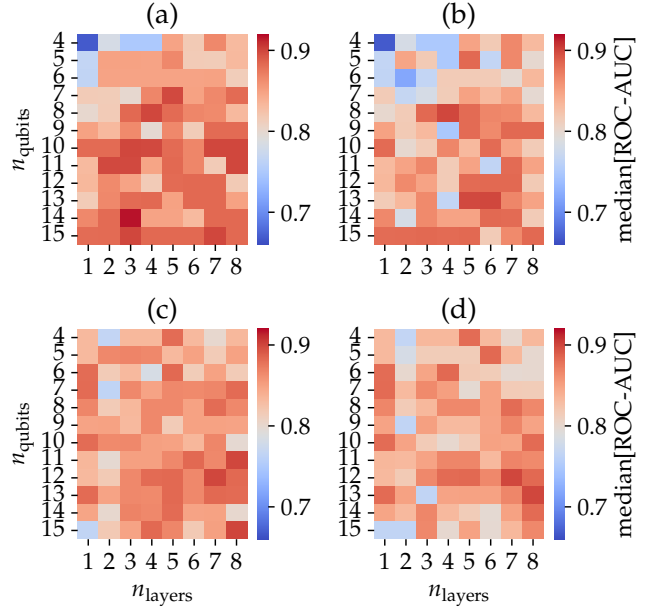


FIG. 11. Investigation of different encoding strategies as illustrated in Fig. 9 for FQK- and PQK-QSVC approaches, respectively for the two curves diff classification dataset with $D = 13$. Note, the feature dimension is kept constant at $d = 4$. The results were aggregated over the respective encoding circuits and then the median of the ROC-AUC test scores was calculated in each case. The upper panel corresponds to FQKs, while the lower panel shows PQKs, whereas the left column represents “option 1” and the right column “option 2”, respectively. As such, we have: (a) FQK, option 1, (b) FQK, option 2, (c) PQK, option 1 and (d) PQK, option 2.

the best of our knowledge, a thorough investigation of these aspects, aside from Ref. [37], which considers the impact of the RDM size k on cross-validation accuracy and generalization ability, is still lacking.

In the following, we systematically examine, for specific datasets from the dataset families considered, the impact of Gaussian, Matérn, and RationalQuadratic outer kernel functions κ , as well as the effects of different measurement operators as defined in Eqs. (14), (16), and (18) on model performance. This includes the Friedman dataset with $n = 10$, QFMNIST with $n = 8$, and the NH₃-PES dataset with $n = 6$ in the case of regression, and for classification problems, the two curves diff and hidden manifold diff datasets with $D = m = 13$ and number of features $d = 4$ respectively. We note that although redundant encoding of some or all features may be beneficial, as shown in the previous section, we restrict ourselves in the following to a number of qubits equal to the number of features in each respective dataset for simplicity. This approach also seems appropriate for answering our research questions.

An overview of the model performance for each of these datasets across the different outer kernel functions per O^k , aggregated over the encoding circuits considered here, is

provided in Appendix D3, with Fig. A16 showing regression tasks and Fig. A17 illustrating classification problems. Here, we aim to quantify the influence of the respective choices on the model performance, while taking into account the corresponding impact of all other hyperparameters. For this purpose, we aggregate all simulation results per dataset and conduct (semi-) partial correlation analyses (cf. Appendix. A for details). The results are summarized in Tab. I. Note that while negative correlation coefficients w.r.t. the MSE point at overall better model performance, it is the other way round for correlations with ROC-AUC scores. To grasp these results illustratively, we once more refer to the supporting Figs. A16 and A17 and the corresponding explanations there. From the pure numbers, we directly realize that both κ and the choice of O^k for calculating the respective projected quantum circuits exhibit statistically significant correlations. For the outer kernel, no universal statement can be made *a priori* regarding which one is generally suitable for effective QKM design—at least not within the scope of our study. The only exception is that for the classification tasks considered here, the RationalQuadratic kernel is not a good choice. Furthermore, it is worth noting that the commonly used vanilla PQQ in the literature, i.e., with a Gaussian kernel, is not automatically the best choice.

In relation to a proper choice of the measurement operator O^k , again there appears to be no *ad-hoc* answer towards which one is best suited to achieve good model performance. Only $X_{k=1}$ seems to be generally insufficient, wherefore we frequently observed training kernel Gram matrices filled entirely with ones, thus rendering them impractical for learning. In contrast, Tab. I suggests a potential improvement in model performance when utilizing the P^{1+2} measurement operator; cf. Eq. (18).

Apart from that, the results indicate that the definition of the projected quantum circuits via O^k , as well as the choice of κ should be considered as additional hyperparameters for PQQ model design. Furthermore, the varying results between each dataset may suggest that this hyperparameter search and thus the fundamental definition of PQQs should be again dataset-driven; analogous to the data encoding circuit architecture search. A systematic investigation of this is however still lacking. But in case this is being confirmed, the correlating significance in relation to the promised benefits of PQQs in regard to circumventing the curse of dimensionality of FQKs [16] requires further exploration.

In Ref. [34] the authors have raised the question whether the projected quantum circuit is not so much responsible for learning, but rather the subsequent outer (Gaussian) kernel applied to the features computed by Eq. (7). To this end, referring first to Tab. I, it becomes evident, as previously discussed, that both the choice of O^k (and thus the projected quantum circuit itself), and the outer kernel κ are crucial for achieving sufficiently good model performance, depending on the dataset. Therefore, the question of which factor is more important cannot be definitively

answered based on this analysis alone. Consequently, we further list all (statistically significant) correlations of the various hyperparameters of the QKMs for a given outer kernel, both among themselves and with model performance in Appendix D3 in Tab. II. Thereof, it again becomes clear that depending on the dataset and outer kernel function, both hyperparameters that contribute to the definition of the projected quantum circuits (i.e., n_{layers} and w_e) and those solely associated with the outer kernel exhibit statistically significant correlations.

To better understand these findings we quantify the distance between Gram matrices G with normalized entries $G_{ij} = k(\mathbf{x}, \mathbf{x}')$ [34]

$$d(G|G') = \frac{\sum_{ij} (G_{ij} - G'_{ij})^2}{|G|}, \quad (19)$$

where $|G|$ refers to the number of entries in G . For Gaussian outer kernels it directly follows from Eq. (9) that the projected quantum circuit contribution $F_{\theta}(\mathbf{x}, \mathbf{x}')$ becomes

$$F_{\theta}(\mathbf{x}, \mathbf{x}') = -\frac{\log[k_{\theta}^{\text{PQK}}(\mathbf{x}, \mathbf{x}')] }{\gamma}. \quad (20)$$

Thus, calculating $d(G|G')$ also defines a difference measure between projected quantum circuit contribution F and F' , which moreover also holds for the Matérn and RationalQuadratic outer kernels, cf. Eqs. (12) and (13), respectively. Figure 12 exemplifies this for the QFMNIST ($n = 8$) dataset for Gaussian outer kernel function. Each section in the central $d(G|G')$ heat map plot corresponds to a family of projected quantum circuits defined by a given measurement operator O^k and is further subdivided into the different encoding circuits in the order as they appear in Appendix B. There are both regions with finite distances between two Gram matrices and those with vanishing differences. This can be explained considering the $\text{Var}(F)$ plot at the top as well as the enlarged examples of the F matrices leading to the respective $d(G|G')$ entries. Vanishing $d(G|G')$ distances correspond to Gram- and F -matrices that show favourable variance behavior or, in other words, lead to similar embedding F and F' in the corresponding Hilbert space (upper zoom-in plot). In contrast, finite distances (lower zoom-in plot) result from one Gram-/ F -matrix being ill-conditioned, i.e., $\text{var}(G) \rightarrow 0$ and thus $\text{var}(F) \rightarrow 0$ or vice versa. Consequently, these matrices correspond to weakly performing (in the sense of MSE scores for regression) models, while the others show better MSE scores, as can be inferred from the respective plot on the right. By considering the w_e - and γ -plots on the left and on the bottom, respectively helps to understand the mechanisms which render these cases into the weak-performing regime. Here, w_e becomes comparatively small, while γ becomes relatively large. With this mechanism we can *a posteriori* explain the origin of bad performing PQQ models in Figs. 6 and 7.

The analogous plots for all datasets as well as for the

TABLE I. Overview of *semi-partial* correlation analysis results for exploring the effect of the choice of the outer kernel function κ (cf. (8)) and the measurement operator O^k (cf. Eqs. (14), (16), (18)) in the definition of a PQK on the resulting test performance scores, while controlling for the effect of all other hyperparameters on the test performance. We investigate PQK-QSVC and PQK-QSVR models for classification and regression tasks, respectively. We compute ROC-AUC scores for evaluating classification accuracy and MSEs for assessing regression results. We employ Spearman ρ rank-order correlation analysis as implemented in the `pingouin` [59] package. Bold values refer to **statistically significant correlations**, with p -values ≤ 0.05 , while others refer to *not* statistically significant correlation, which are given for the sake of completeness. We note that while negative correlation coefficients w.r.t. the MSE point at overall better model performance, it is the other way round for correlations with ROC-AUC scores.

dataset	$\rho_{\text{Spearman}}^{\kappa}$			$\rho_{\text{Spearman}}^{O_k}$								
	κ^{Gauss}	$\kappa_{3/2}^{\text{Mat}}$	κ^{RQ}	$X_{k=1}$	$Z_{k=1}$	$X_{k=1} + Z_{k=1}$	$\sum_P P_{k=1}$	$X_{k=2}$	$Z_{k=2}$	$X_{k=2} + Z_{k=2}$	$\sum_P P_{k=2}$	P^{1+2}
<i>correlations w.r.t. MSE</i>												
Friedman ($n = 10$)	-0.063	0.126	-0.068	0.237	0.183	-0.031	-0.220	0.187	0.087	0.012	-0.102	-0.352
QFMNIST ($n = 8$)	0.129	-0.09	0.045	0.129	0.107	-0.086	-0.097	0.113	0.057	-0.040	-0.051	-0.139
NH ₃ -PES	-0.265	0.261	-0.036	0.245	0.049	-0.040	-0.084	0.106	-0.022	0.056	-0.125	-0.203
<i>correlations w.r.t. ROC-AUC</i>												
two curves diff ($D = 13$)	-0.297	0.394	-0.115	-0.340	-0.125	0.038	0.191	-0.265	0.020	0.012	0.210	0.256
hidden manifold diff ($m = 13$)	0.188	0.038	-0.215	-0.149	-0.020	-0.007	-0.077	-0.086	0.036	0.025	0.166	0.113

remaining outer kernel functions are detailed in the Appendix D in Figs. A18 to A31.

Eventually, this analysis (as well as Eq. (20) and analogous relations for Matérn and RationalQuadratic outer kernels) confirms our hypothesis that there is a synergy and dependence between projected quantum circuits and outer kernel as well as QKM hyperparameters. As such, also given the insights from Tabs. I and II, we conclude that both parts are responsible for learning.

V. DISCUSSION

In this benchmarking study, we systematically analyzed various design criteria of QKMs based on both FQKs and PQKs for several regression and classification tasks. In order to gain deeper insights into the functional principles underlying QKMs and derive universal insights, we conducted hyperparameter optimizations and training of more than 20,000 models. However, although we attempted to encompass multiple different dataset families, the effective number of distinct families, the size of each dataset, and the specifics of splitting them into training and test sets represents a restriction, which limits the generalizability of our results.

The study of hyperparameter importances for effective model tuning illustrated that regularization, length scale (for PQKs) and data prescaling hyperparameters, are mostly driving the successful training of QKMs within our simulations. These results further indicated that the number of qubits and layers of the respective data encoding circuits are less important, both for FQK and PQK approaches. Given that for increasing dataset complexity, in particular for the two classification tasks considered here, the number of qubits and layers for successful QKM training may become more relevant, the pronounced importance of these classical hyperparameters found here

can probably be attributed to the (low) difficulty of some of the dataset configurations. In this respect, it is known that quantum models can be written as partial Fourier series in the data, where the accessible frequencies are eventually determined by the number of qubits and layers of the underlying data encoding circuits [14]. Moreover, while Ref. [11] outlines the Fourier representation of quantum kernels, it remains an interesting question how this can be leveraged for the QKM design as well as for the identification of promising dataset properties.

Moreover, our analysis of model performances demonstrated that the average feature correlation to the targets can serve as a useful difficulty measure for predicting test performance scores. We generally found that as dataset complexity increases, the higher/lower the MSE/ROC-AUC metrics, respectively. Interestingly, for regression tasks the particular choice of kernel method, i.e., QKRR and QSVR approaches is not really important as, on average, they are performing equally well. Similarly, our experiments across both regression and classification tasks, show no significant performance differences between FQK and PQK, even though we simulate up to 15 qubits. In this range, the first effects of the limited trainability of FQKs due to the exponential concentration phenomenon [28] should appear, and one might expect evidence of better PQK performance. The absence of this observation however, may be explained by bandwidth tuning (here, we optimize w_e), whereby generalizability can be established, but, as shown in Refs. [29, 37], at the expense of becoming classically tractable. To properly understand the connections between bandwidth tuning, exponential concentration and classical tractability in terms of the geometric difference metric [16] will be part of a future work. Our Spearman correlation analyses further validated the importance of classical hyperparameters, aligning with our findings from the hyperparameter importance study.

Another remarkable observation from our explorations

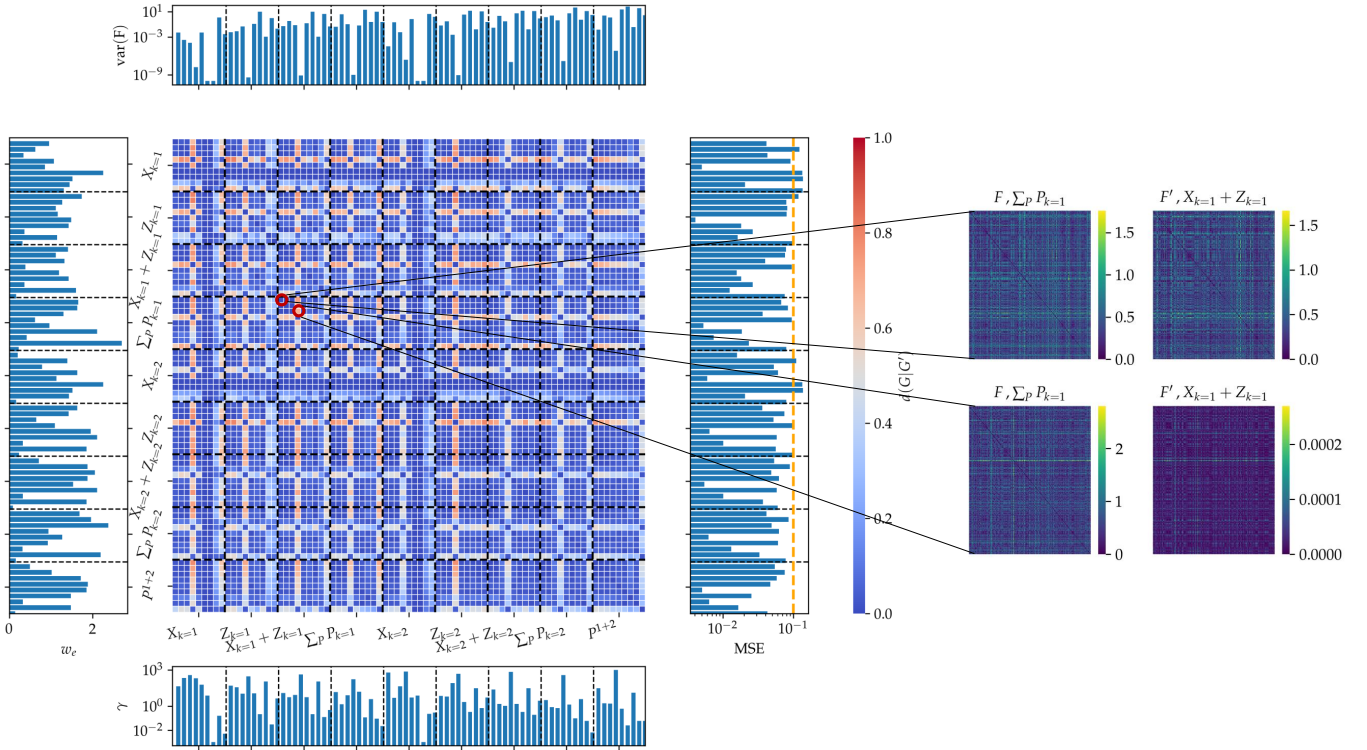


FIG. 12. Comprehensive insight into various mechanisms of PQKs exemplified for the QFMNIST dataset with $n = 8$ principal components and Gaussian outer kernel function. The central heatmap plot illustrates the $d(G|G')$ distance measure according to Eq. (19), where each section corresponds to a family of projected quantum circuits as defined by a given measurement operator O^k . The sections are further subdivided into the different encoding circuits in the order as they appear in Appendix B. The plot at the top details $\text{Var}(F)$; cf. Eq. (20). The close-up images on the very right correspond to examples of F and F' matrices that lead to $d(G|G') \rightarrow 0$ and $d(G|G') \neq 0$, respectively. The F matrices can be viewed as illustrations of embeddings into the corresponding Hilbert space. The histogram of MSEs right to the central heatmap helps to identify Gram matrices that lead to good/bad performances, respectively. The w_e - and γ -plots on the left and on the bottom, respectively, help to understand the mechanisms which render these cases into the weak-performing regime. Here, w_e becomes comparatively small, while γ becomes relatively large.

confirms Ref. [34] and demonstrates that data encoding circuits without entanglement perform well. Based on our results, we are inclined to stress this even more to that extent that encoding circuits without entanglement perform equally well or better than those with entangling gates. This holds for FQKs and PQKs as well as for QSVM and QKRR approaches in regression and classification tasks, respectively, highlighting the need to unravel the driving forces of QKM performance if “quantumness” turns out as a debatable mechanism.

We note that although we have randomly initialized the trainable parameters of data encoding circuits, they resulted in comparatively good performance scores in all cases. Although the influence of tuning these variational parameters has not been investigated systematically in this study, we found in some cases that training them can improve the QKM performance, although there is no guaranty, cf. Appendix E. Hence, we recommend to carefully scrutinize this in future studies.

The survey of different data encoding strategies in terms

of embedding some or all features redundantly, revealed that for regression tasks based on FQKs it is beneficial to redundantly encode all features on a number of qubits that is given by integer multiples of the number of features. For PQKs redundant embedding appears to be negligible. For the classification tasks considered in this work, we observed best performances for both FQK and PQK for a number of qubits corresponding to non-integer multiples of the number of features.

Our exploration of PQK design options, including the effect of various measurement operators and outer kernel functions, hinted at that projected quantum circuits and classical hyperparameters, particularly regularization strengths, data prescaling, and length scale parameters, work synergistically to drive learning. However, these findings as well as those resulting from detailed correlation analyses indicate that our understanding of “quantumness” of QKMs can be challenged even further, apart from the already mentioned entanglement problem. At this we note that investigating shadow kernels or linear PQKs [16] accordingly remains open.

Concerning proper datasets for QKM tasks, our results for QFMNIST, which can be seen as artificially engineered quantum data, may be interpreted such that there is some weak indicative that the actual quantum part of QKMs, i.e., the number of qubits and layers of the data encoding circuits as well as the choice of the measurement operator in case of PQK become slightly more important.

In conclusion we believe that this study, substantially contribute to better understand what distinguished good from bad QKMs. For the datasets we investigated in this work, we showed that in most cases it remains unresolved to clearly reveal the quantum contribution and its importance for learning. At most for PQKs we could reveal that classical and quantum parts can contribute likewise. In our view, these findings corroborate the need to tackle QML research from two sides, i.e. identify requirements for datasets with potential quantum advantage and explore how corresponding model design should look like.

ACKNOWLEDGMENTS

This work was supported by the German Federal Ministry of Economic Affairs and Climate Action through the project AQUAS (grant no. 01MQ22003D), as well as the German Federal Ministry of Education and Research through the project H2Giga Degrad-EL³ (grant no. 03HY110D). Furthermore, the authors acknowledge Fraunhofer IAO for providing access to the GPU simulation cluster (CLARSA), which was established as part of the Competence Center Quantum Computing Baden-Württemberg. Here, J.S. is grateful to Vamshi Mohan Katukuri for his support with and excellent administration of the computing clusters. Furthermore, we would like to thank Moritz Link for his excellent contributions in an early stage of this work. Moreover, we are particularly grateful for insightful discussions with Roberto Flórez Ablan.

-
- [1] J. Biamonte, P. Wittek, N. Pancotti, P. Rebentrost, N. Wiebe, and S. Lloyd, Quantum machine learning, *Nature* **549**, 195 (2017).
- [2] M. Cerezo, G. Verdon, H.-Y. Huang, L. Cincio, and P. J. Coles, Challenges and opportunities in quantum machine learning, *Nature Computational Science* **2**, 567 (2022).
- [3] M. Schuld and N. Killoran, Quantum machine learning in feature hilbert spaces, *Phys. Rev. Lett.* **122**, 040504 (2019).
- [4] V. Havlíček, A. D. Córcoles, K. Temme, A. W. Harrow, A. Kandala, J. M. Chow, and J. M. Gambetta, Supervised learning with quantum-enhanced feature spaces, *Nature* **567**, 209 (2019).
- [5] E. Peters, J. Caldeira, A. Ho, S. Leichenauer, M. Mohseni, H. Neven, P. Spentzouris, D. Strain, and G. N. Perdue, Machine learning of high dimensional data on a noisy quantum processor, *npj Quantum Information* **7**, 161 (2021).
- [6] T. Tomono and S. Natsubori, Performance of quantum kernel on initial learning process, *EPJ Quantum Technology* **9**, 35.
- [7] T. Hubregtzen, D. Wierichs, E. Gil-Fuster, P.-J. H. S. Derks, P. K. Faehrmann, and J. J. Meyer, Training quantum embedding kernels on near-term quantum computers, *Phys. Rev. A* **106**, 042431 (2022).
- [8] S. Jerbi, L. J. Fiderer, H. Poulsen Nautrup, J. M. Kübler, H. J. Briegel, and V. Dunjko, Quantum machine learning beyond kernel methods, *Nat. Commun.* **14**, 517 (2023).
- [9] B. Y. Gan, D. Leykam, and S. Thanasilp, *A unified framework for trace-induced quantum kernels* (2023).
- [10] Y. Liu, S. Arunachalam, and K. Temme, A rigorous and robust quantum speed-up in supervised machine learning, *Nature Physics* **17**, 1013 (2021).
- [11] M. Schuld, *Supervised quantum machine learning models are kernel methods* (2021).
- [12] B. Schölkopf and A. Smola, *Learning with Kernels: Support Vector Machines, Regularization, Optimization, and Beyond*, Adaptive computation and machine learning (MIT Press, 2002).
- [13] S. Lloyd, M. Schuld, A. Ijaz, J. Izaac, and N. Killoran, *Quantum embeddings for machine learning* (2020).
- [14] M. Schuld, R. Sweke, and J. J. Meyer, The effect of data encoding on the expressive power of variational quantum-machine-learning models, *Phys. Rev. A* **103**, 032430 (2021).
- [15] C. Blank, D. K. Park, J.-K. K. Rhee, and F. Petruccione, Quantum classifier with tailored quantum kernel, *npj Quantum Information* **6**, 41 (2020).
- [16] H.-Y. Huang, M. Broughton, M. Mohseni, R. Babbush, S. Boixo, H. Neven, and J. Mcclean, Power of data in quantum machine learning, *Nature Communications* **12** (2021).
- [17] Y. Suzuki and M. Li, *Effect of alternating layered ansatzes on trainability of projected quantum kernel* (2023).
- [18] S. Miyabe, B. Quanz, N. Shimada, A. Mitra, T. Yamamoto, V. Rastunkov, D. Alevras, M. Metcalf, D. J. M. King, M. Mamouei, M. D. Jackson, M. Brown, P. Intalura, and J.-E. Park, *Quantum multiple kernel learning in financial classification tasks* (2023).
- [19] B. Djehiche and B. Löfdahl, Quantum support vector regression for disability insurance, *Risks* **9**, 10.3390/risks9120216 (2021).
- [20] A. E. Paine, V. E. Elfving, and O. Kyriienko, Quantum kernel methods for solving regression problems and differential equations, *Phys. Rev. A* **107**, 032428 (2023).
- [21] T. Hubregtzen, J. Pichlmeier, P. Stecher, and K. Bertels, Evaluation of parametrized quantum circuits: on the relation between classification accuracy, expressibility, and entangling capability, *Quantum Machine Intelligence* **3**, 9 (2021).
- [22] D. Sharma, P. Singh, and A. Kumar, The role of entanglement for enhancing the efficiency of quantum kernels towards classification, *Physica A: Statistical Mechanics and its Applications* **625**, 128938 (2023).
- [23] M. John, J. Schuhmacher, P. Barkoutsos, I. Tavernelli, and F. Tacchino, Optimizing quantum classification algorithms on classical benchmark datasets, *Entropy* **25**, 10.3390/e25060860 (2023).

- [24] F. Rapp, D. A. Kreplin, and M. Roth, [Reinforcement learning-based architecture search for quantum machine learning](#) (2024).
- [25] J. Kübler, S. Buchholz, and B. Schölkopf, The inductive bias of quantum kernels, in *Advances in Neural Information Processing Systems*, Vol. 34, edited by M. Ranzato, A. Beygelzimer, Y. Dauphin, P. Liang, and J. W. Vaughan (Curran Associates, Inc., 2021) pp. 12661–12673.
- [26] R. Shaydulin and S. M. Wild, Importance of kernel bandwidth in quantum machine learning, *Phys. Rev. A* **106**, 042407 (2022).
- [27] A. Canatar, E. Peters, C. Pehlevan, S. M. Wild, and R. Shaydulin, [Bandwidth enables generalization in quantum kernel models](#) (2023).
- [28] T. Supanut, W. Samson, M. Cerezo, and Z. Holmes, Exponential concentration in quantum kernel methods, *Nat. Commun.* **15**, 5200 (2024).
- [29] L. Slattery, R. Shaydulin, S. Chakrabarti, M. Pistoia, S. Khairy, and S. M. Wild, Numerical evidence against advantage with quantum fidelity kernels on classical data, *Phys. Rev. A* **107**, 062417 (2023).
- [30] J. Schnabel, [Qkmtuner](#) (2024), version 0.0.1.
- [31] D. A. Kreplin, M. Willmann, J. Schnabel, F. Rapp, M. Hagelüken, and M. Roth, [sqlearn – a python library for quantum machine learning](#) (2024).
- [32] T. Akiba, S. Sano, T. Yanase, T. Ohta, and M. Koyama, Optuna: A next-generation hyperparameter optimization framework, in *Proceedings of the 25th ACM SIGKDD International Conference on Knowledge Discovery and Data Mining* (Association for Computing Machinery, New York, NY, USA, 2019).
- [33] F. Pedregosa, G. Varoquaux, A. Gramfort, V. Michel, B. Thirion, O. Grisel, M. Blondel, P. Prettenhofer, R. Weiss, V. Dubourg, J. Vanderplas, A. Passos, D. Cournapeau, M. Brucher, M. Perrot, and E. Duchesnay, Scikit-learn: Machine learning in Python, *Journal of Machine Learning Research* **12**, 2825 (2011).
- [34] J. Bowles, S. Ahmed, and M. Schuld, [Better than classical? the subtle art of benchmarking quantum machine learning models](#) (2024).
- [35] C. Moussa, Y. J. Patel, V. Dunjko, T. Bäck, and J. N. van Rij, Hyperparameter importance and optimization of quantum neural networks across small datasets, *Machine Learning* **113**, 1941 (2024).
- [36] M. Kashif, M. Rashid, S. Al-Kuwari, and M. Shafique, [Alleviating barren plateaus in parameterized quantum machine learning circuits: Investigating advanced parameter initialization strategies](#) (2023).
- [37] S. Egginger, A. Sakhnenko, and J. M. Lorenz, A hyperparameter study for quantum kernel methods, *Quantum Machine Intelligence* **6**, 44 (2024).
- [38] N. Aronszajn, Theory of reproducing kernels, *Trans. Amer. Math. Soc.* **68**, 337 (1950).
- [39] B. Schölkopf, R. Herbrich, and A. J. Smola, A generalized representer theorem, in *Computational Learning Theory*, edited by D. Helmbold and B. Williamson (Springer Berlin Heidelberg, Berlin, Heidelberg, 2001) pp. 416–426.
- [40] F. Di Marcantonio, M. Incudini, D. Tezza, and M. Grossi, Quantum advantage seeker with kernels (QuASK): a software framework to speed up the research in quantum machine learning, *Quantum Machine Intelligence* **5**, 10.1007/s42484-023-00107-2 (2023).
- [41] C. E. Rasmussen and C. K. William, *Gaussian Processes for Machine Learning* (The MIT Press, 2005).
- [42] K. A. Murphy, *Machine Learning: A probabilistic perspective* (The MIT Press, 2012).
- [43] S. Altares-López, A. Ribeiro, and J. J. García-Ripoll, Automatic design of quantum feature maps, *Quantum Science and Technology* **6**, 045015 (2021).
- [44] T. Haug, C. N. Self, and M. S. Kim, Quantum machine learning of large datasets using randomized measurements, *Machine Learning: Science and Technology* **4**, 015005 (2023).
- [45] D. A. Kreplin and M. Roth, Reduction of finite sampling noise in quantum neural networks, *Quantum* **8**, 1385 (2024).
- [46] A. Javadi-Abhari, M. Treinish, K. Krsulich, C. J. Wood, J. Lishman, J. Gacon, S. Martiel, P. D. Nation, L. S. Bishop, A. W. Cross, B. R. Johnson, and J. M. Gambetta, *Quantum computing with Qiskit* (2024).
- [47] S. Buchanan, D. Gilboa, and J. Wright, [Deep networks and the multiple manifold problem](#) (2021).
- [48] S. Goldt, M. Mézard, F. Krzakala, and L. Zdeborová, Modeling the influence of data structure on learning in neural networks: The hidden manifold model, *Phys. Rev. X* **10**, 041044 (2020).
- [49] A. C. Lorena, A. I. Maciel, P. B. C. de Miranda, I. G. Costa, and R. B. C. Prudêncio, Data complexity meta-features for regression problems, *Machine Learning* **107**, 209 (2018).
- [50] A. C. Lorena, L. P. F. Garcia, J. Lehmann, M. C. P. Souto, and T. K. Ho, How complex is your classification problem? a survey on measuring classification complexity, *ACM Comput. Surv.* **52**, 10.1145/3347711 (2019).
- [51] J. H. Friedman, Multivariate Adaptive Regression Splines, *The Annals of Statistics* **19**, 1 (1991).
- [52] L. Breiman, Bagging predictors, *Machine Learning* **24**, 123 (1996).
- [53] H. Xiao, K. Rasul, and R. Vollgraf, [Fashion-mnist: a novel image dataset for benchmarking machine learning algorithms](#) (2017).
- [54] G. A. Schmitz, [Machine Learning for Potential Energy Surface Construction: A Benchmark Set](#) (2019).
- [55] V. Bergholm, J. Izaac, M. Schuld, C. Gogolin, S. Ahmed, V. Ajith, M. S. Alam, G. Alonso-Linaje, B. Akash-Narayanan, A. Asadi, J. M. Arrazola, U. Azad, S. Banning, C. Blank, T. R. Bromley, B. A. Cordier, J. Ceroni, A. Delgado, O. D. Matteo, A. Dusko, T. Garg, D. Guala, A. Hayes, R. Hill, A. Ijaz, T. Isacsson, D. Ittah, S. Jhangiri, P. Jain, E. Jiang, A. Khandelwal, K. Kottmann, R. A. Lang, C. Lee, T. Loke, A. Lowe, K. McKiernan, J. J. Meyer, J. A. Montañez-Barrera, R. Moyard, Z. Niu, L. J. O’Riordan, S. Oud, A. Panigrahi, C.-Y. Park, D. Polatajko, N. Quesada, C. Roberts, N. Sá, I. Schoch, B. Shi, S. Shu, S. Sim, A. Singh, I. Strandberg, J. Soni, A. Száva, S. Thabet, R. A. Vargas-Hernández, T. Vincent, N. Vitucci, M. Weber, D. Wierichs, R. Wiersema, M. Willmann, V. Wong, S. Zhang, and N. Killoran, [Pennylane: Automatic differentiation of hybrid quantum-classical computations](#) (2022).
- [56] D. Duvenaud, [The kernel cookbook: Advice on covariance functions](#) (2014), accessed: 27.07.2024.
- [57] S. Watanabe, [Tree-structured parzen estimator: Understanding its algorithm components and their roles for better empirical performance](#) (2023).
- [58] F. Hutter, H. Hoos, and K. Leyton-Brown, An efficient approach for assessing hyperparameter importance, in *Proceedings of the 31st International Conference on Machine Learning*

- Learning*, Proceedings of Machine Learning Research, Vol. 32, edited by E. P. Xing and T. Jebara (PMLR, Beijing, China, 2014) pp. 754–762.
- [59] R. Vallat, Pingouin: statistics in python, [Journal of Open Source Software](#) **3**, 1026 (2018).
 - [60] S. Kim, ppcor: An r package for a fast calculation to semi-partial correlation coefficients, [Communications for Statistical Applications and Methods](#) **22**, 665 (2015).
 - [61] D. Alvarez-Estevez, [Benchmarking quantum machine learning kernel training for classification tasks](#) (2024).

APPENDICES

Appendix A: Some background on statistical methods

Since we subject our results a statistical analysis to detect statistically significant correlations between hyperparameters and hyperparameters and model performance, we briefly describe the underlying concepts in the following.

Correlation analysis is a statistical technique used to measure and describe the strength and direction of the relationship between two variables. The Pearson and Spearman correlation coefficients are two primary types of quantifying correlation. The *Pearson* correlation coefficient measures the linear relationship between two datasets X and Y . Strictly speaking, Pearson's correlation requires each dataset to be normally distributed as well as assumes homoscedasticity, i.e., the spread of the data points is consistent across the range of values. It is [59]

$$r = \frac{\sum_i (x_i - \bar{x})(y_i - \bar{y})}{\sqrt{\sum_i (x_i - \bar{x})^2} \sqrt{\sum_i (y_i - \bar{y})^2}}, \quad (\text{A1})$$

where $x_i \in X$ and $y_i \in Y$ are the individual sample points, while \bar{x} and \bar{y} are the means for the $x_i \in X$ and $y_i \in Y$ samples, respectively. Correlations of ± 1 imply a perfect positive and negative linear relationship, respectively, with 0 indicating the absence of association. The *Spearman* correlation coefficient is a non-parametric measure of the monotonicity of the relationship between two datasets. Unlike the Pearson correlation it does not assume that both datasets are normally distributed. Correlations ± 1 imply an exact positive and negative monotonic relationship, respectively. Mathematically, the Spearman correlation coefficient is defined as the Pearson correlation coefficient between the rank variables. The Spearman's rank correlation is moreover less sensitive to outliers.

To obtain reliable correlation estimates it is crucial to ensure a sufficiently large sample size. Additionally, one should ideally ensure that inferred correlation coefficients are statistically significant. This can be done by computing p-values. The p-value is the probability of obtaining a correlation coefficient as extreme as, or more extreme than the observed value under the null hypothesis H_0 , which assumes that there is no correlation between the two variables. For interpreting p-values in correlation analysis one defines a significance level, which is commonly set to 0.001, 0.01 or 0.05. Then it holds

- $p \leq 0.05$: The correlation is statistically significant and one can reject H_0
- $p > 0.05$: The correlation is *not* statistically significant and one fails to reject H_0 .

Typically one performs two-sided statistical tests to compute the p -value, i.e., it checks for the H_0 and for an alternative hypothesis H_1 , assuming the correlation is

different from zero. It is important to adjust the p -values accordingly to account for increased risk of false positives. There are several methods available, for more details we refer to the documentation of the python package `pingoin` [59].

Another essential concept of correlation analysis are *partial correlations* [60] to measure the degree of association between two variables x and y while controlling for the effect of one or more additional variables z . This helps to isolate the direct relationship between two primary variables of interest, removing the influence of the control variables. Practically, this is achieved by calculating the correlation coefficient between the residuals of two linear regressions [59]

$$x \sim z, y \sim z. \quad (\text{A2})$$

Like the correlation coefficient, the partial correlation coefficient takes on a value in $[-1, 1]$. The semi-partial correlation works analogously, with the exception that the set of controlling variables in only removes from either x or y .

Appendix B: Detailed overview of encoding circuits

In the following we provide plots of each encoding circuits used in this study and briefly describe (cf. `sQLearn` documentation) the corresponding features. Features are denoted with a feature vector $\mathbf{x}[i]$, while variationally trainable parameters (θ) are labeled $p[i]$.

1. YZ_CX_EncodingCircuit

This encoding circuit was introduced in Ref. [44] and is originally designed for encoding high-dimensional features. An example with four qubits and features and two layers is shown in Fig. A1.

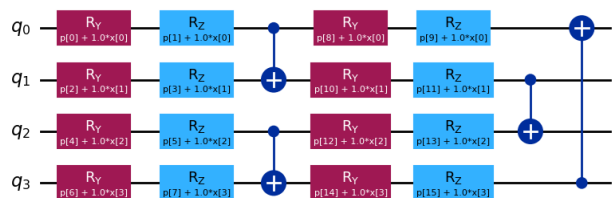


FIG. A1. Exemplaric illustration of the `YZ_CX_EncodingCircuit` from Ref. [44].

2. HighDimEncodingCircuit

The `HighDimEncodingCircuit` from Ref. [5], was introduced to deal with high-dimensional data from the domain

of cosmology and is constructed such that it preserves the magnitude of the entries of the quantum kernel matrix that otherwise typically vanish due to the exponentially growing Hilbert space. An example with four qubits and four features as well as two layers is depicted in Fig. A2.

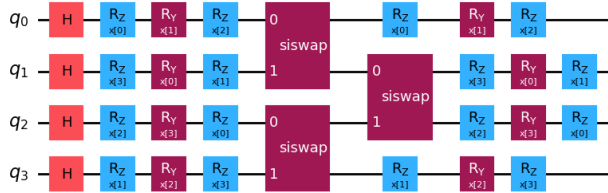


FIG. A2. Exemplaric representation of the HighDimEncodingCircuit from Ref. [5].

3. HZY_CZ_EncodingCircuit

This encoding circuit was introduced in Ref. [7] and is shown exemplarily in Fig. A3 for four qubits, four features and two layers.

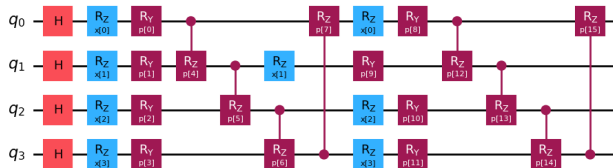


FIG. A3. Exemplaric representation of the HZY_CZ_EncodingCircuit from Ref. [21].

4. ChebyshevPQC

The ChebyshevPQC encoding circuit was introduced in Ref. [45] to provide a basis of Chebyshev polynomials. This is realized by the non-linear feature encodings via $\arccos(x)$ mappings. In the mentioned paper it was shown that this data encoding works well within a QNN setting. An example illustration with four qubits, four features and two layers is given in Fig. A4.

5. ParamZFeatureMap

This encoding circuit is inspired by Qiskit's ZFeatureMap and allows for rescaling the input data with variationally trainable parameters and introduces additional CNOT gates between the default rotation gates. An example is given in Fig. A5.

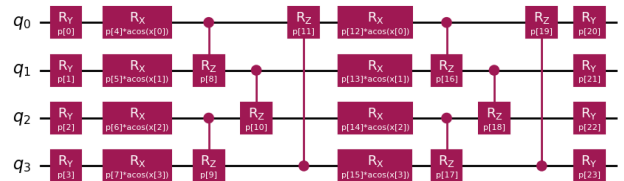


FIG. A4. Exemplaric representation of the ChebyshevPQC as introduced in Ref. [45].

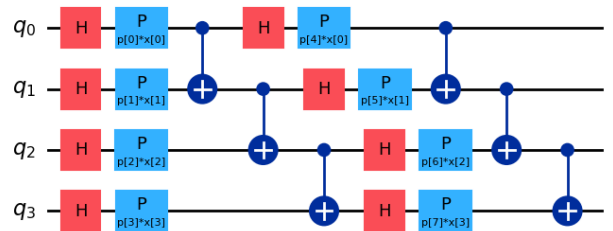


FIG. A5. Exemplaric representation of the ParamZFeatureMap, which implements Qiskit's ZFeatureMap with additional CNOT gates between the rotation layers.

6. SeparableEncodingRx

This paradigmatic encoding circuit was used in Ref. [27] to analytically study the effect of bandwidth tuning in quantum kernels. In this work, we include this data encoding to reveal learning capabilities of QKMs in absence of entanglement. An example is shown in Fig. A6.

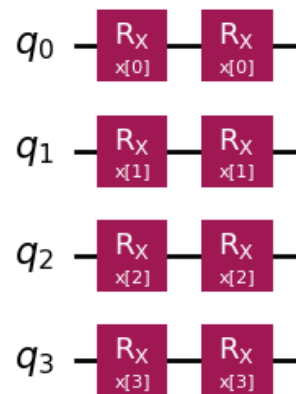


FIG. A6. Exemplaric representation of the SeparableRxEncoding from Ref. [27].

7. HardwareEfficientEmbeddingRx

The `HardwareEfficientEmbeddingRx` circuit is taken from Ref. [28], where it served as basis to study exponential concentration in QKMs. An example is shown in Fig. A7.

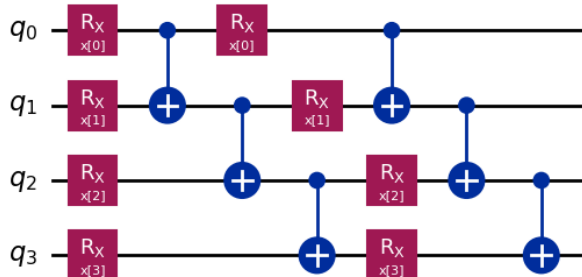


FIG. A7. Exemplaric representation of the `HardwareEfficientEmbeddingRx` from Ref. [28].

8. ZFeatureMap

This encoding circuit is taken from Qiskit [46]. It defines a first-order Pauli-Z-evolution circuit. An example is given in Fig. A8.

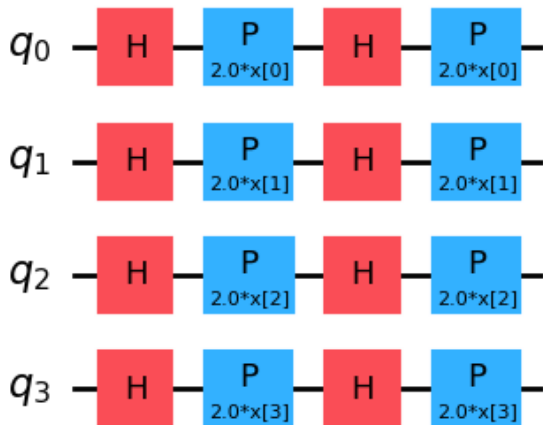


FIG. A8. Exemplaric representation of Qiskit’s `ZFeatureMap`, cf. Ref. [46].

9. ZZFeatureMap

This encoding circuit is taken from Qiskit [46]. It defines a second-order Pauli-Z-evolution circuit. An example is given in Fig. A9.

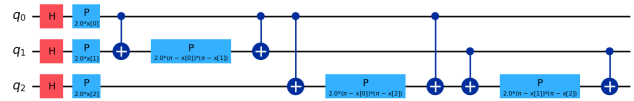


FIG. A9. Exemplaric representation of Qiskit’s `ZZFeatureMap`, cf. Ref. [46].

Appendix C: Note on reproducibility of results

To ensure reproducible results across executions, we set the `random_state` parameter of *scikit-learn*’s estimators and splitters. Here, we follow the recommendations in the *scikit-learn* documentation on robustness of cross-validation results; i.e., we pass a `RandomState` instance to the estimator (here `QSVC` is the only one with a `random_state` parameter) while we pass an integer to the cross-validation and the train-test splitters. Regarding the latter, we note that comprehensively validating the stability of results would require to test different inter-ger seeds. In our case, this is infeasible due to the enormous study size. However, since we aim at unravling general patterns and trends in QKMs, we do not require to pinpoint individual model performances and hence the necessity of stabilizing results across differents seed is not that important.

Appendix D: Detailed Results

Here we support and complement the key findings of this study as presented in Sec. IV of the main text.

1. Details on model performance and correlation analysis

In Sec. IV B we mention that both regression and classification datasets exhibit a propensity for overfitting. The Friedman and QFMNIST regression datasets in Figs. A10 (a) and (b), respectively, reveal that each dataset (in terms of n) shows lower whiskers with $\text{MSE} \rightarrow 0$. Comparing to the corresponding test performance scores in Figs. 6 (a) and (b), this may also indicate signatures of overfitting especially for datasets with larger n . In this respect, one should carefully investigate different training- and test set sizes, which represents a limiting factor of this study. The corresponding training performance scores for the two curves diff and hidden manifold diff datasets are displayed in Figs. A10 (c) and (d), respectively.

When investigating the impact of data encoding circuits on QKM model performance, we merely presented results of the Friedman (regression) and the two curves diff (classification) datasets in Fig. 7. Here, we provide analogue findings in Fig. A11 for the QFMNIST and the hidden

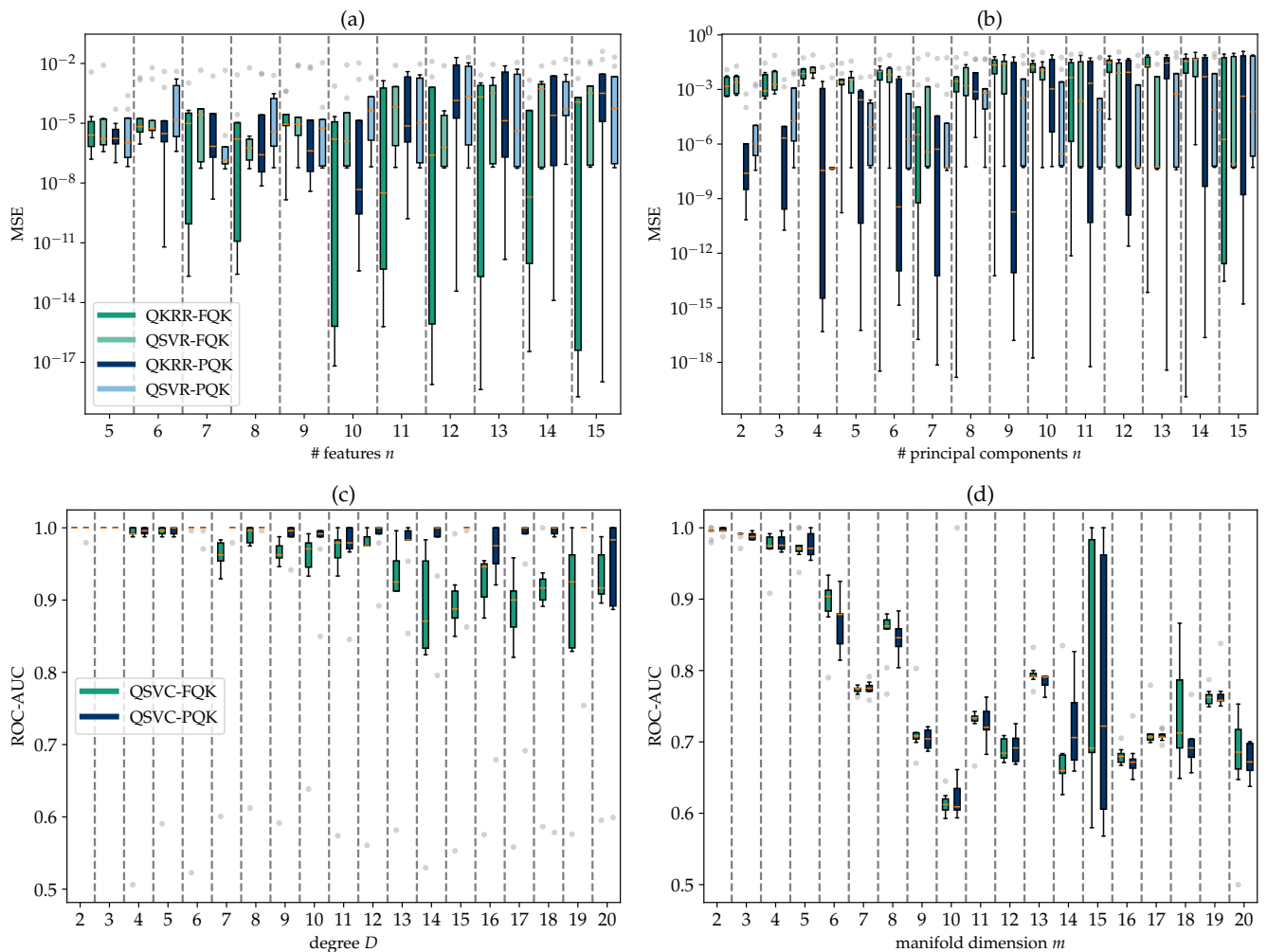


FIG. A10. Analogous illustration to Fig. 6 with associated *training* performance scores. Results for each QKM and dataset are aggregated across data encoding circuits with corresponding optimal n_{layers}^* , yielding minimum/maximum test performance scores for regression/classification, respectively. The **upper panel** displays corresponding findings for **regression** datasets. Here, (a) shows the **Friedman** dataset family with datasets for $\# \text{features } n = [5, 15]$. In (b) we give results corresponding to the **QFMNIST** dataset family with datasets having number of principal components $n = [2, 15]$. The **lower panel** shows the **classification** tasks. The results in (c) correspond to the **two curves diff** family with $d = 4$ and degree $D = [2, 20]$. In (d) we present the **hidden manifold diff** family with $d = 4$ and manifold dimension $m = [2, 20]$.

manifold diff datasets.

Finally, we summarize those results of the correlation analyses between QKM hyperparameters and test performance scores, as well as between the hyperparameter themselves, that are not shown in the main text in Sec. IV B in the following Fig. A12.

2. Details on data encoding strategies

The results for testing the two different encoding strategies for the Friedman dataset for $n = 5$ features as outlined in the main text, cf. Sec. IV C and Fig. 9, are displayed in Fig. A13. Contrary to the QFMNIST results in Fig. 10, in all cases, except for FQK, option 2, most accurate

results are obtained for $n_{\text{qubits}} = 12$. Here, FQK and PQK approaches show similar behavior. The second encoding option for FQK appears to be less sensitive for the respective feature redundancy. Notably, that the redundancy does not have to be an integer multiple of the original number of features.

Figure A14 shows the result for testing the two different encoding strategies for the NH_3 dataset. Most accurate results are obtained for integer multiples of the number of features. Figure A15 provides insights into the effect of the two different encoding strategies for the hidden manifold diff dataset with $m = 13$. The findings discussed for the two curves diff dataset in Sec. IV C still apply.

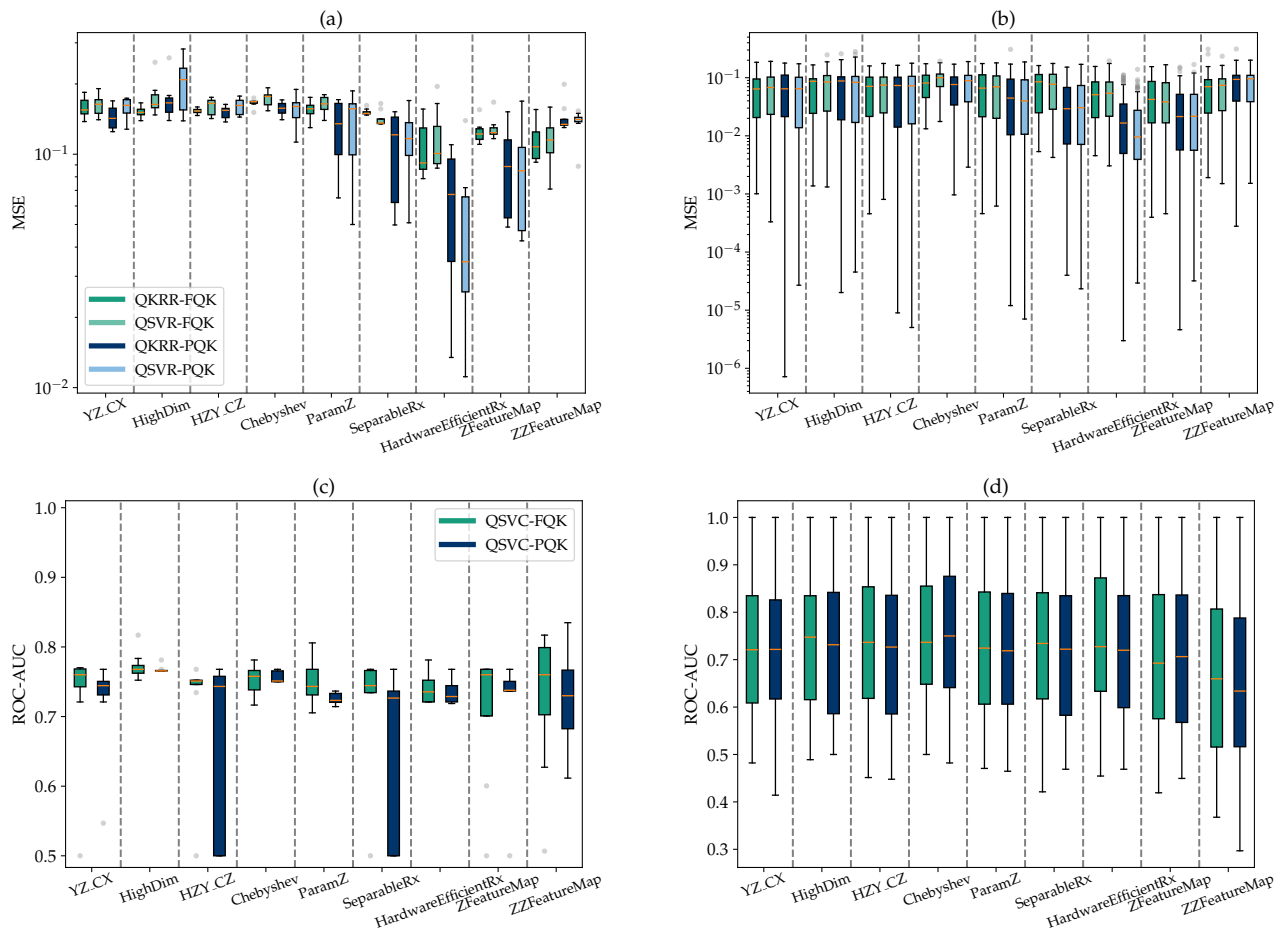


FIG. A11. Complementing illustration to Fig. 7 of the main text with the datasets not shown therein. **Upper panel:** Regression QFMNIST. With (a) Test performance aggregated over $n_{\text{layers}} \in [1, 8]$ per regression method (QSVR/QKRR) and quantum kernel for the dataset with number of features $n = 15$ and (b) test performance scores aggregated over all datasets in the QFMNIST family and over respective n_{layers} . **Lower panel:** hidden manifold diff. With (c) Test performance aggregated over $n_{\text{layers}} \in [1, 8]$ for the dataset with manifold dimension $m = 13$ and (d) test performance scores aggregated over all datasets in the hidden manifold diff family and over respective n_{layers} .

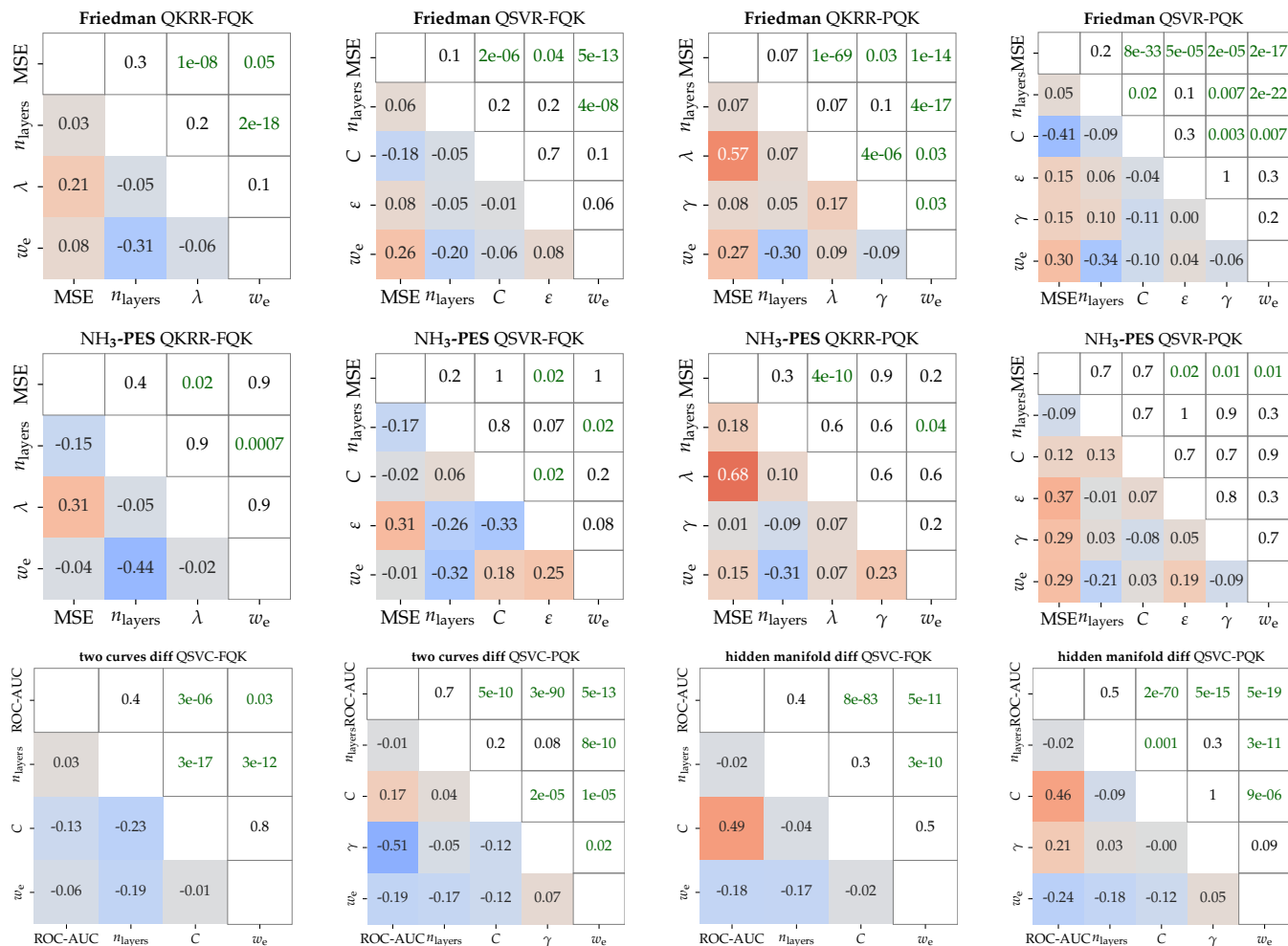


FIG. A12. Summary of the Spearman correlation analyses between QKM hyperparameters and test performance scores, as well as between the hyperparameters themselves as discussed in Sec. IV B. This figure complements the respective discussion in the main text with the findings for the other datasets. The results correspond to aggregating data across all datasets within the associated family, encoding circuits, and $n_{\text{layers}} \in [1, 8]$. The Spearman correlation coefficients are given on the lower triangles of the respective matrices (with blue for negative to red for positive coefficients), while the upper triangles display corresponding p -values. Here, statistically significant correlations ($p \leq 0.05$) are highlighted in green. Since we use the MSE to evaluate regression performance and the ROC-AUC score for classification, we note that the signs of respective correlation coefficient work in opposite direction; i.e., e.g., negative correlation with MSE means better regression performance, while it is the other way round for classification. The **first row** corresponds to **Friedman** and the **second row** to the **NH₃-PES** regression tasks. The **third row** illustrates **two curves diff** on the left and **hidden manifold diff** on the right.

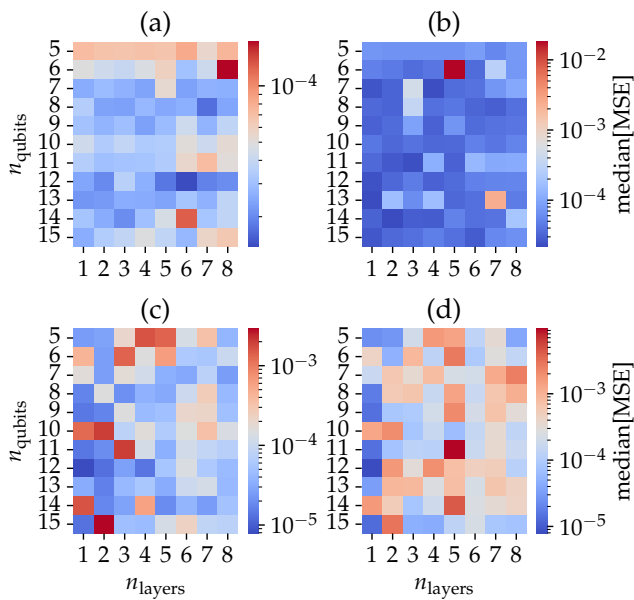


FIG. A13. Investigation of different encoding strategies as illustrated in Fig. 9 for FQK and PQK approaches for the Friedman regression dataset $n = 5$ features. The results were aggregated over QKRR and QSVR approaches as well as over the corresponding encoding circuits, and then the median of the MSE test scores was calculated in each case. The upper panel corresponds to FQKs, while the lower panel shows PQKs, whereas the left column represents “option 1” and the right column “option 2”, respectively. As such, we have: (a) FQK, option 1, (b) FQK, option 2, (c) PQK, option 1 and (d) PQK, option 2.

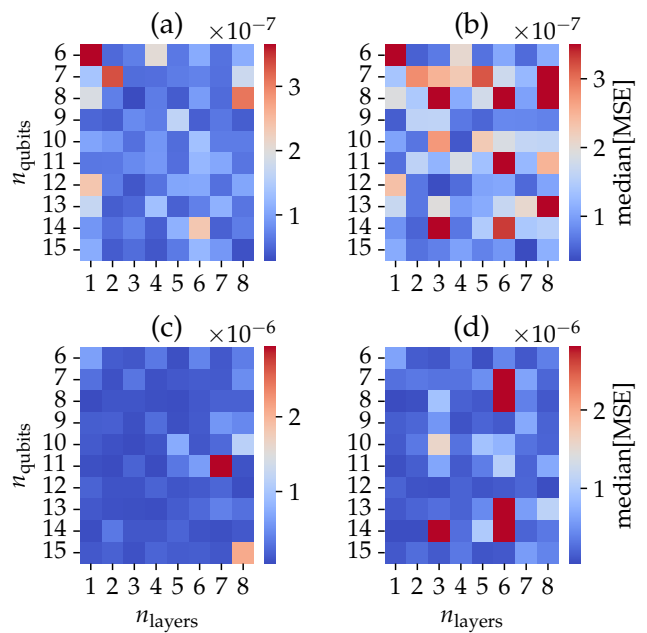


FIG. A14. Investigation of different encoding strategies as illustrated in Fig. 9 for FQK and PQK approaches for the NH_3 regression dataset (number of features = 6). The results were aggregated over QKRR and QSVR approaches as well as over the corresponding encoding circuits, and then the median of the MSE test scores was calculated in each case. The upper panel corresponds to FQKs, while the lower panel shows PQKs, whereas the left column represents “option 1” and the right column “option 2”, respectively. As such, we have: (a) FQK, option 1, (b) FQK, option 2, (c) PQK, option 1 and (d) PQK, option 2.

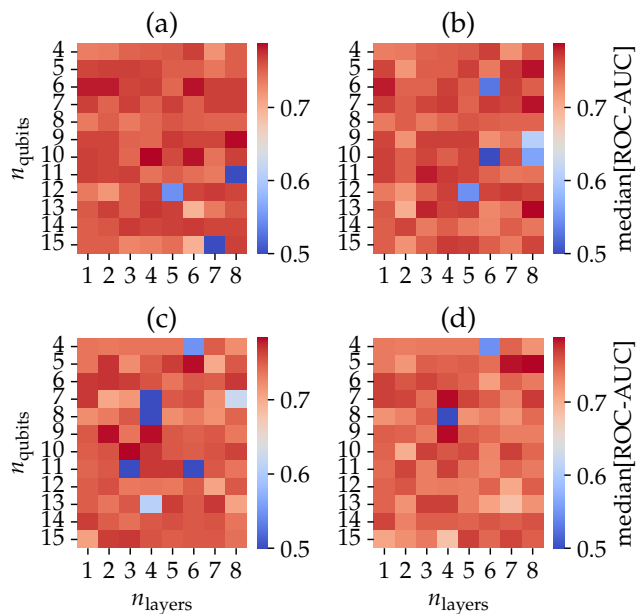


FIG. A15. Investigation of different encoding strategies as illustrated in Fig. 9 for FQK- and PQK-QSVC approaches, respectively for the hidden manifold diff classification dataset with manifold dimension $m = 13$. Note, the feature dimension is kept constant at $d = 4$. The results were aggregated over the respective encoding circuits and then the median of the ROC-AUC test scores was calculated in each case. The upper panel corresponds to FQKs, while the lower panel shows PQKs, whereas the left column represents “option 1” and the right column “option 2”, respectively. As such, we have: (a) FQK, option 1, (b) FQK, option 2, (c) PQK, option 1 and (d) PQK, option 2.

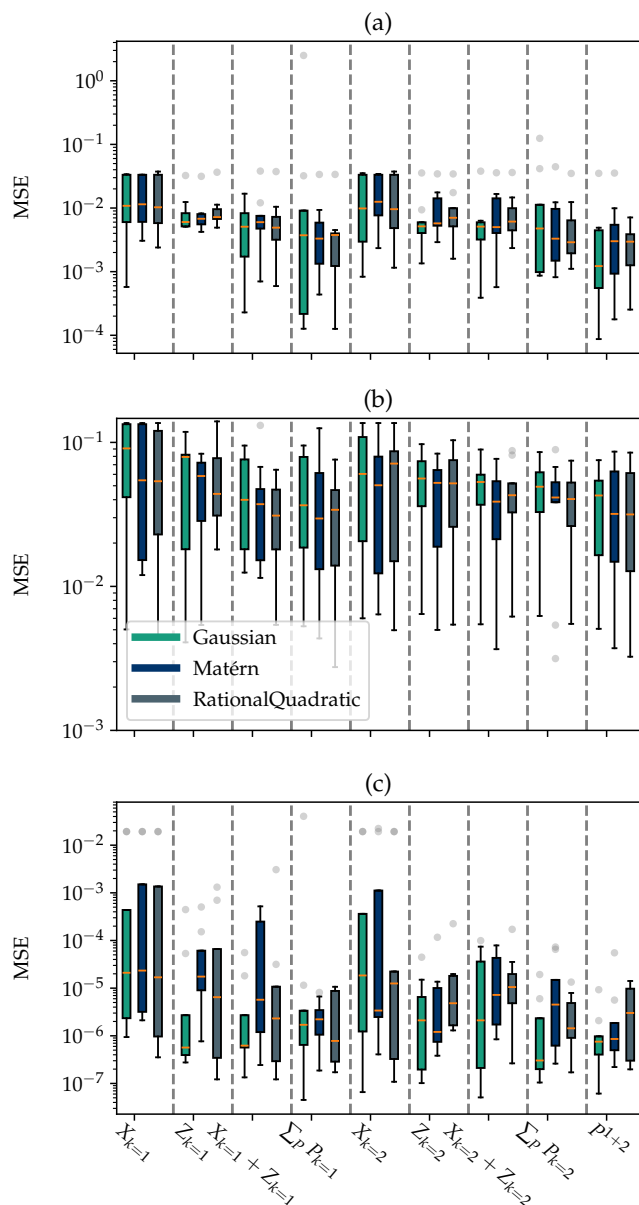


FIG. A16. MSE on test data as a function of the measurement operators given in Eqs. (14), (16) and (18) for Gaussian, Matérn and RationalQuadratic outer kernel functions κ . (a) Friedman dataset for $n = 10$ features. (b) QFMNIST for $n = 8$ PCA components. (c) The NH_3 -PES. The data for each O^k are aggregated across the encoding circuits considered in this work.

3. Details on in-depth analysis of PQK design options

a. Overview on test performances

In the main text we investigate (semi-) partial correlations in Tabs. I and II between the choice of the outer kernel function κ and corresponding hyperparameters as well as the measurement operator O^k and resulting model

test performances. In the following, we give a detailed insights into the test scores for each outer kernel (Gaussian, Matérn, RationalQuadratic) as a function of the measurement operator in Figs. A16 and A17 for the regression and classification tasks, respectively considered in this study. The data for each O^k are aggregated across the encoding circuits considered here. Comparing these plots with the numbers listed in Tab. I helps to understand the reported statistically significant correlation. For instance, Fig. A16 (b) indicates that for each O^k the Gaussian outer kernel leads to weaker test performance scores compared to the rest. This in turn reflects in the positive Spearman correlation coefficient in Tab. I. Analogous conclusions can be drawn for the observed trends with respect to the different measurement operators considered in this work.

The same applies to, e.g., the two curves diff dataset in Fig. A17 (a). While the Gaussian kernel tends to yield relatively low ROC-AUC scores, the Matérn kernel generally shows a trend towards higher test scores. Again, this reflects in the negative and positive, respectively Spearman correlation coefficients in Tab. I. Once more, we note that analogous implications hold for findings regarding the different measurement operators.

b. Extended correlation analysis

In order to support the efforts in Sec. IVD to gain a deeper understanding of what are basic mechanisms in PQKs responsible for learning, we provide all (statistically significant) semi-partial correlations of the various hyperparameters of the QSVC/QSVR-PQK model for a given outer kernel κ , both among themselves and with model test performance in Tab. II. Here, we note that while negative correlation coefficients w.r.t. the MSE point at overall better model performance, it is the other way round for correlations with ROC-AUC scores.

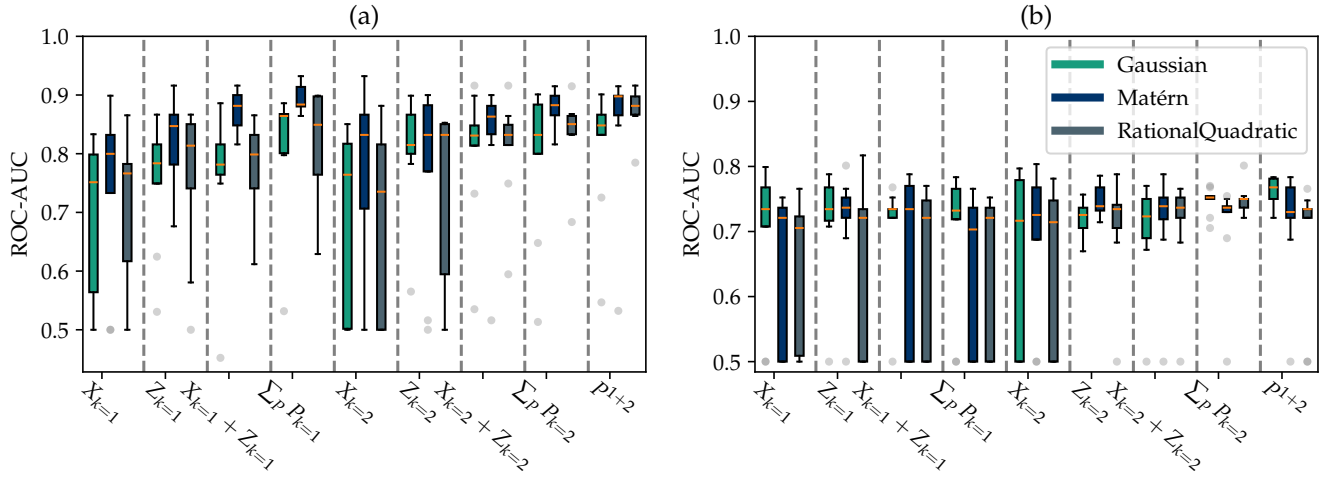


FIG. A17. ROC-AUC test score as a function of the measurement operators given in Eqs. (14), (16) and (18) for Gaussian, Matér and RationalQuadratic outer kernel functions κ . (a) two curves diff dataset for $d = 4$ and degree $D = 13$. (b) hidden manifold diff dataset for $d = 4$ and manifold dimension $m = 13$. The data for each O^k are aggregated across the encoding circuits considered in this work.

TABLE II. Statistically significant semi-partial correlations of the various hyperparameter of the QSVR/QSVC-PQK model for a given outer kernel function κ , both among themselves and with test performance scores. This table supports the corresponding discussion in Ref. IV D. *We note that while negative correlation coefficients w.r.t. the MSE point at overall better model performance, it is the other way round for correlations with ROC-AUC scores.*

κ (Dataset)	X	Y	$\rho_{\text{Spearman}}(X, Y)$
κ^{Gauss} (Friedman)	n_{layers}	γ	0.344
	C	MSE	-0.331
	w_e	MSE	0.267
κ^{Gauss} (QFMNIST)	C	MSE	0.353
	γ	w_e	-0.262
	n_{layers}	γ	0.293
κ^{Gauss} (NH ₃ -PES)	C	ε	0.319
	C	MSE	0.233
	ε	MSE	0.390
	w_e	MSE	0.322
κ^{Gauss} (two curves diff)	n_{layers}	γ	-0.270
	γ	ROC-AUC	-0.306
κ^{Gauss} (hidden manifold diff)	n_{layers}	w_e	-0.264
	w_e	ROC-AUC	-0.355
$\kappa_{3/2}^{\text{Mat}}$ (Friedman)	n_{layers}	C	-0.260
	n_{layers}	w_e	-0.275
	n_{layers}	MSE	0.465
	C	MSE	-0.402
	ε	MSE	0.242
	ℓ	MSE	-0.246
$\kappa_{3/2}^{\text{Mat}}$ (QFMNIST)	n_{layers}	MSE	0.244
	ℓ	w_e	0.337
	n_{layers}	C	0.272
$\kappa_{3/2}^{\text{Mat}}$ (NH ₃ -PES)	ε	MSE	0.250
	ℓ	w_e	0.403
	w_e	MSE	0.228
	C	ℓ	0.490
$\kappa_{3/2}^{\text{Mat}}$ (two curves diff)	C	ROC-AUC	0.323
	ℓ	w_e	0.305
	w_e	ROC-AUC	-0.318
$\kappa_{3/2}^{\text{Mat}}$ (hidden manifold diff)	n_{layers}	ℓ	-0.370
	n_{layers}	w_e	-0.345
	C	ℓ	0.238
κ^{RQ} (Friedman)	w_e	ROC-AUC	-0.299
	n_{layers}	ℓ	-0.290
	C	α	-0.264
	α	ℓ	-0.382
	α	MSE	-0.441
	w_e	MSE	0.254
κ^{RQ} (QFMNIST)	C	α	-0.431
	α	ℓ	-0.263
	ℓ	w_e	0.562
κ^{RQ} (NH ₃ -PES)	C	ℓ	0.365
	ε	MSE	0.281
	α	w_e	0.275
	α	MSE	-0.301
κ^{RQ} (two curves diff)	n_{layers}	C	-0.236
	C	α	-0.304
	α	ℓ	-0.251
	α	w_e	0.312
κ^{RQ} (hidden manifold diff)	ℓ	ROC-AUC	0.473
	n_{layers}	ℓ	-0.341
	n_{layers}	w_e	-0.477
	C	ROC-AUC	0.456
	α	ℓ	0.535
κ^{RQ} (hidden manifold diff)	α	w_e	0.256
	ℓ	ROC-AUC	-0.358
	w_e	ROC-AUC	-0.250

In Sec. IVD we thoroughly investigate the underlying mechanisms that are eventually responsible for learning in PQQ approaches. While comprehensive correlation analyses in Tabs. I and II provide profound insights, a deeper understanding of these findings follows from studying the distance measure as defined in Eq. (19). For Gaussian outer kernels we can additionally define the matrix of the projected quantum circuit contributions F_{θ} as given in Eq. (20). In the main text, we detail the corresponding discussion for the QFMNIST ($n = 8$) dataset in case of the Gaussian outer kernel. The central illustration for this is provided in Fig. 12. Subsequent to these explanations we display the corresponding findings for the Matérn and RationalQuadratic outer kernels in Figs. A18 and A19, respectively. In contrast to studying $\text{var}(F)$ in case of Gaussian outer kernels, we can leverage the analogous notion of $\text{var}(G)$ to explain (non-)vanishing $d(G|G')$ distances. Finite distances result from one Gram matrix being ill-conditioned, i.e., $\text{var}(G) \rightarrow 0$, while vanishing distances correspond to favourable variance behaviors. By considering the feature scaling w_e and length-scale parameters (ℓ and α) on the left and on the bottom, respectively helps to understand the mechanisms that render these cases into the weak-performing regime.

Similarly, we explore all remaining datasets of this study and provide corresponding plots as follows:

- **Friedman** with Gaussian, Matérn and RationalQuadratic outer kernels in Figs. A20, A21 and A22
- **NH₃-PES** with Gaussian, Matérn and RationalQuadratic outer kernels in Figs. A23, A24 and A25
- **two curves diff** with Gaussian, Matérn and RationalQuadratic outer kernels in Figs. A26, A27 and A28
- **hidden manifold diff** with Gaussian, Matérn and RationalQuadratic outer kernels in Figs. A29, A30,

Appendix E: Optimization of trainable parameters in data encoding circuits

Here, we provide a brief insight into the optimization of the variational parameters θ , which are generally incorporated for defining data encoding circuits as given in Eq. (3). As mentioned in Sec. III A, these trainable parameters, if present, were randomly initialized with a fixed seed. To study the effectiveness of parameter optimization, we optimize the model corresponding to the best ‘‘ChebyshevPQC’’ configuration for both the two curves diff ($D = 13$), cf. Fig. 7 (c) and the hidden manifold diff ($m = 13$) datasets. For this purpose, the kernel-target-alignment (KTA) metric is maximized over the training set [21, 61]. We employ the respective sQUlearn implementation with the corresponding Adam optimizer.

The results listed in Tab. III indicate that optimization can lead to a significant improvement in the case of the two curves diff dataset, but, this improvement is not guaranteed, as demonstrated by the counterexample of the hidden manifold diff dataset. This discrepancy may be attributed to a poorly tuned optimizer. A detailed analysis of this issue, as well as the investigation of a broader range of datasets and data encoding circuits, however, is beyond the scope of this work. Nevertheless, we highlight the potential of KTA optimization for datasets with high complexity with correlating sub-optimal QKMs.

TABLE III. KTA results for two curves diff ($D = 13$) and hidden manifold diff ($m = 13$) datasets for both QSVC-FQK and QSVC-PQK approaches. All results correspond to the respective best performing ‘‘ChebyshevPQC’’ encoding circuits.

Dataset	QKM	ROC-AUC before	ROC-AUC after
two curves diff	FQK	0.506	0.801
	PQK	0.682	0.834
hidden manifold diff	FQK	0.781	0.683
	PQK	0.768	0.641

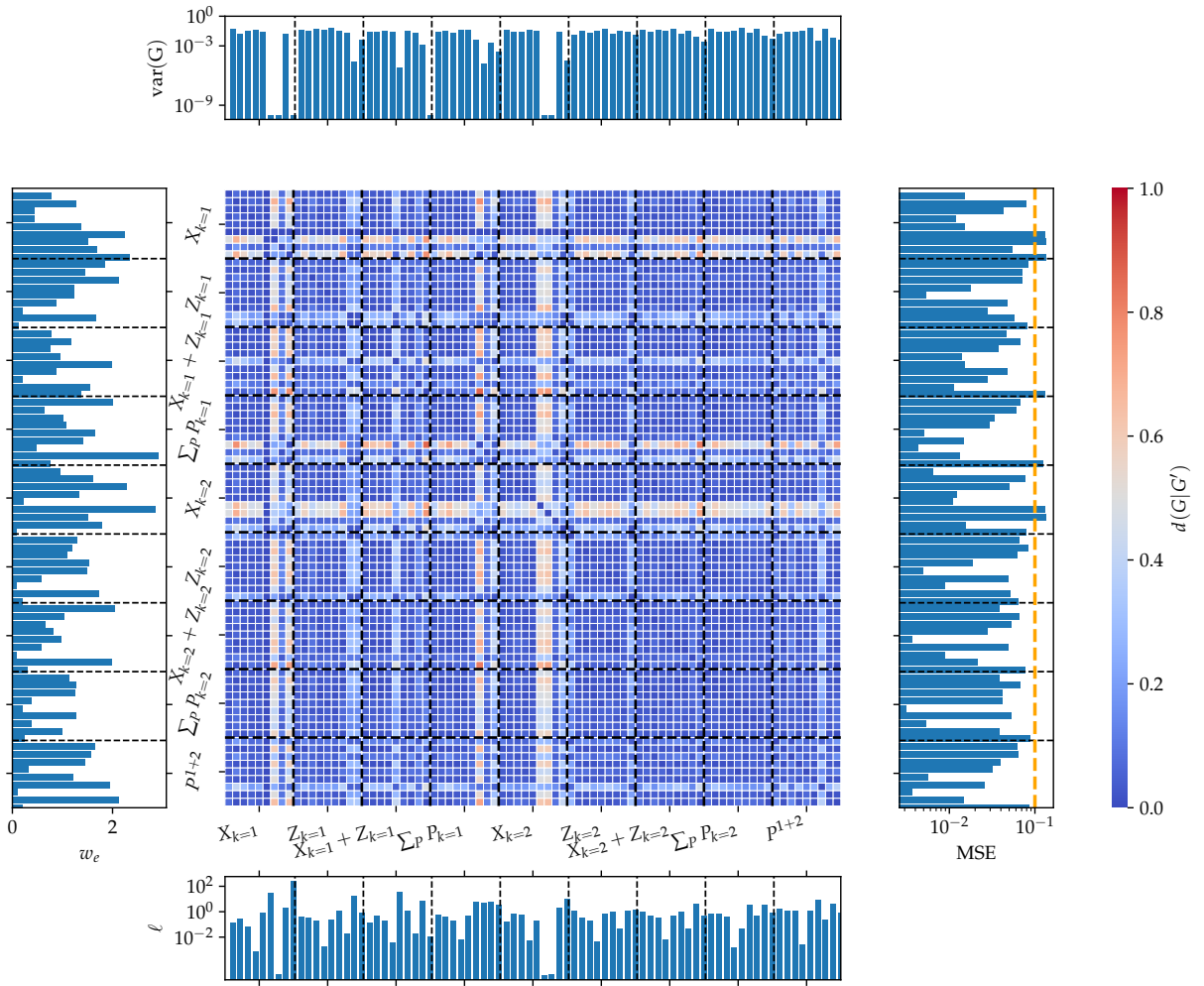


FIG. A18. Analogous illustration to Fig. 12 as discussed in Sec. IV D for the QFMNIST dataset with $n = 8$ components and the Matérn outer kernel.

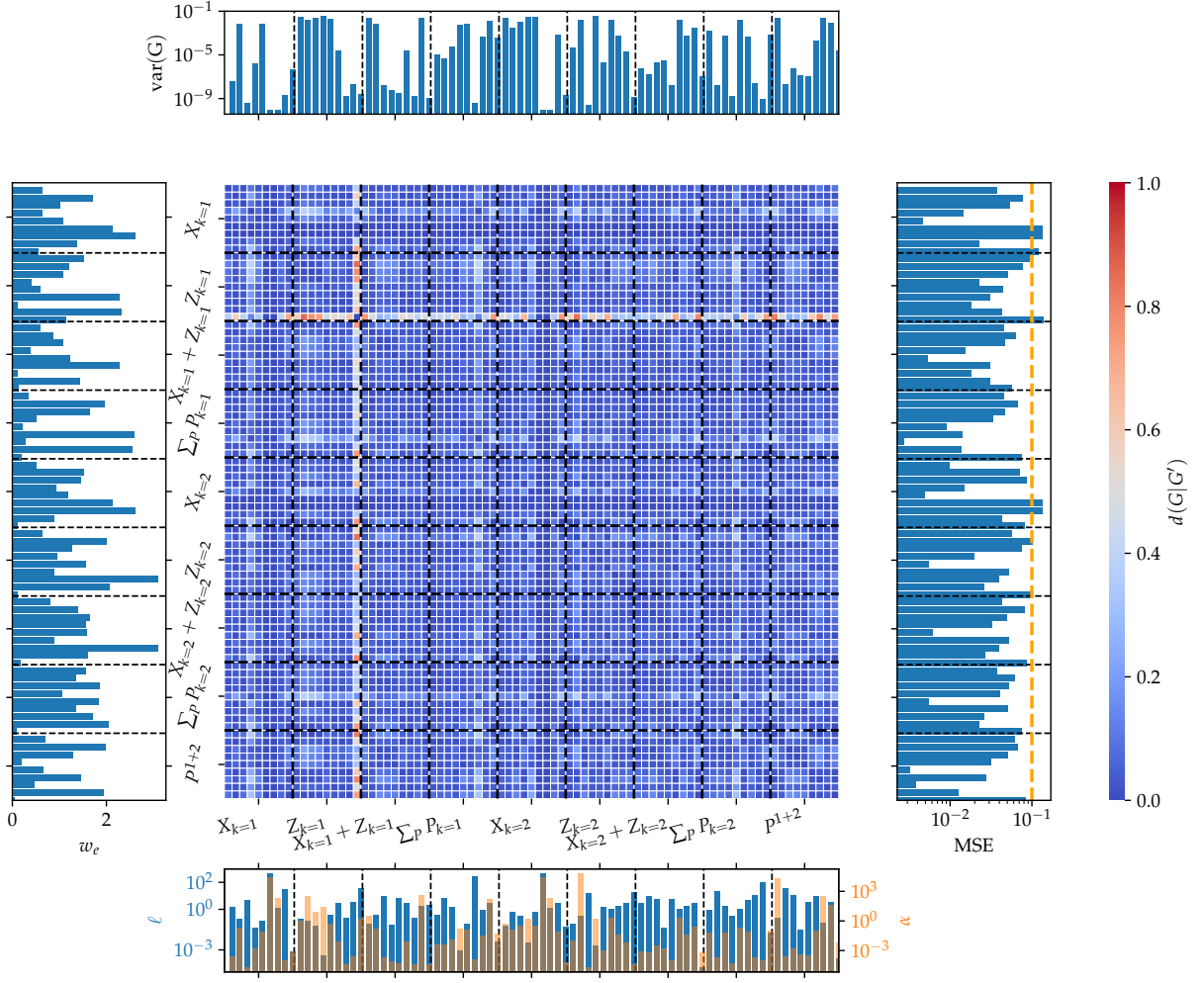


FIG. A19. Analogous illustration to Fig. 12 as discussed in Sec. IV D for the QFMNIST dataset with $n = 8$ components and the RationalQuadratic outer kernel.

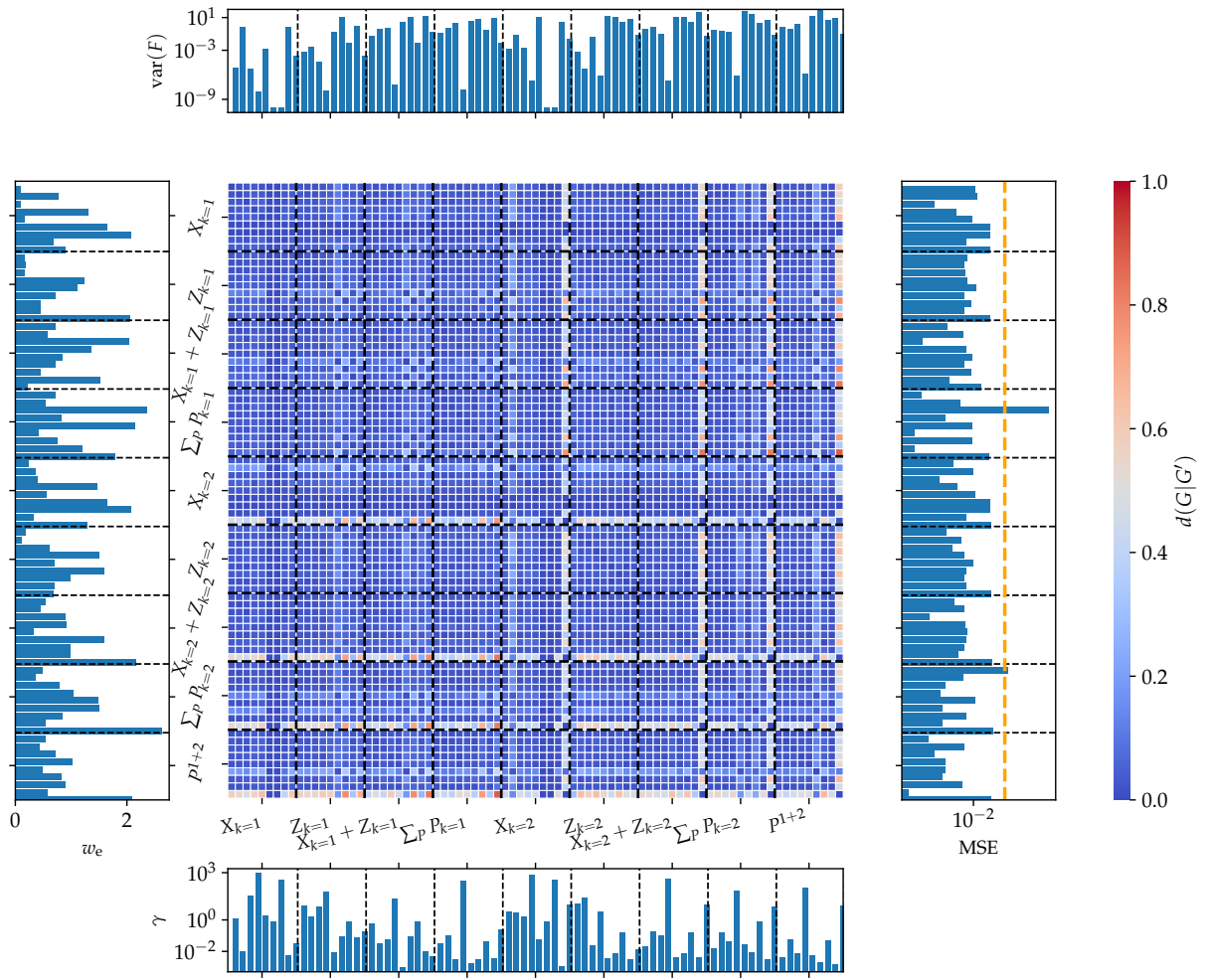


FIG. A20. Analogous illustration to Fig. 12 as discussed in Sec. IVD for the Friedman dataset with $n = 10$ features and the Gaussian outer kernel.

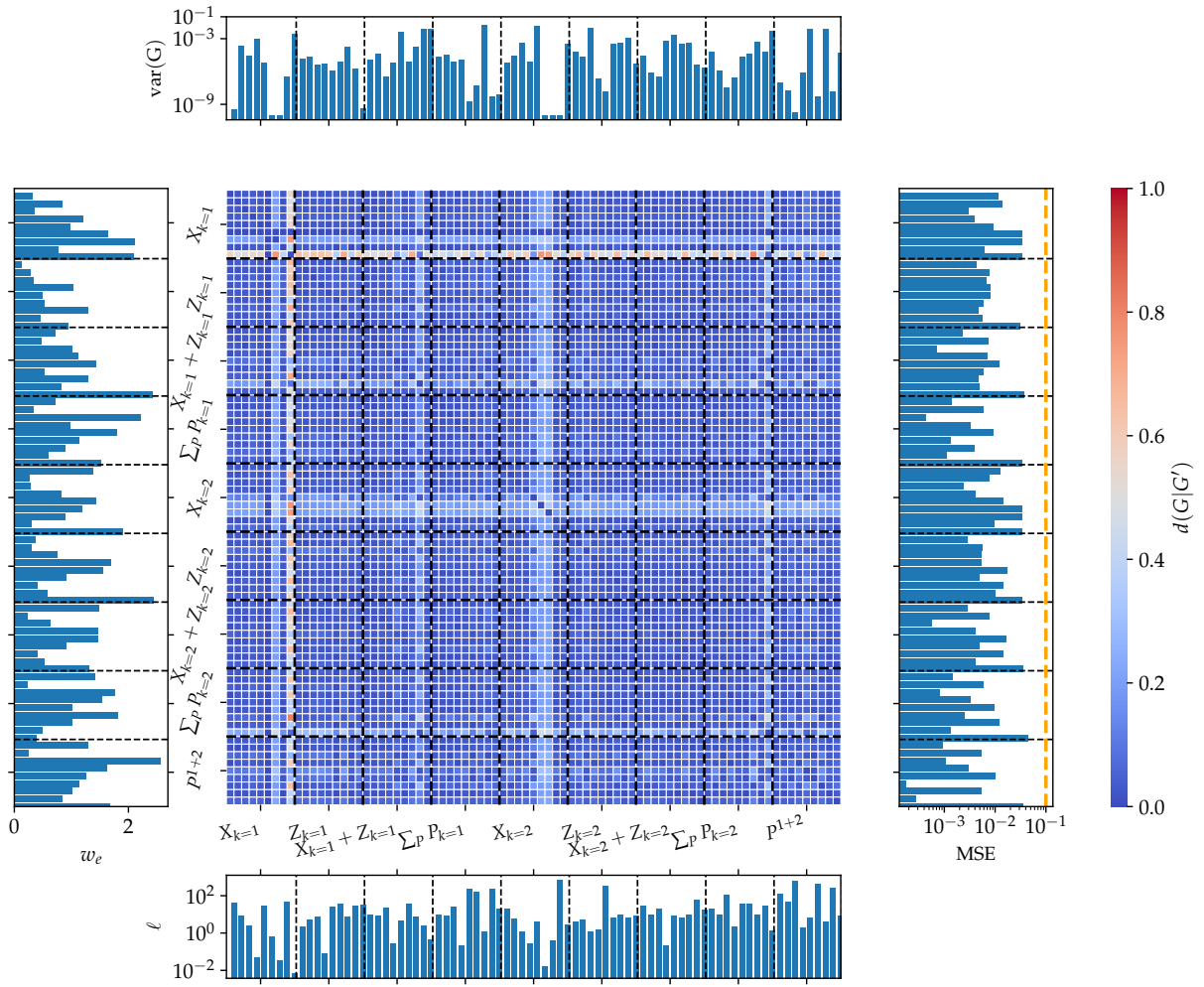


FIG. A21. Analogous illustration to Fig. 12 as discussed in Sec. IV D for the Friedman dataset with $n = 10$ features and the Matérn outer kernel.

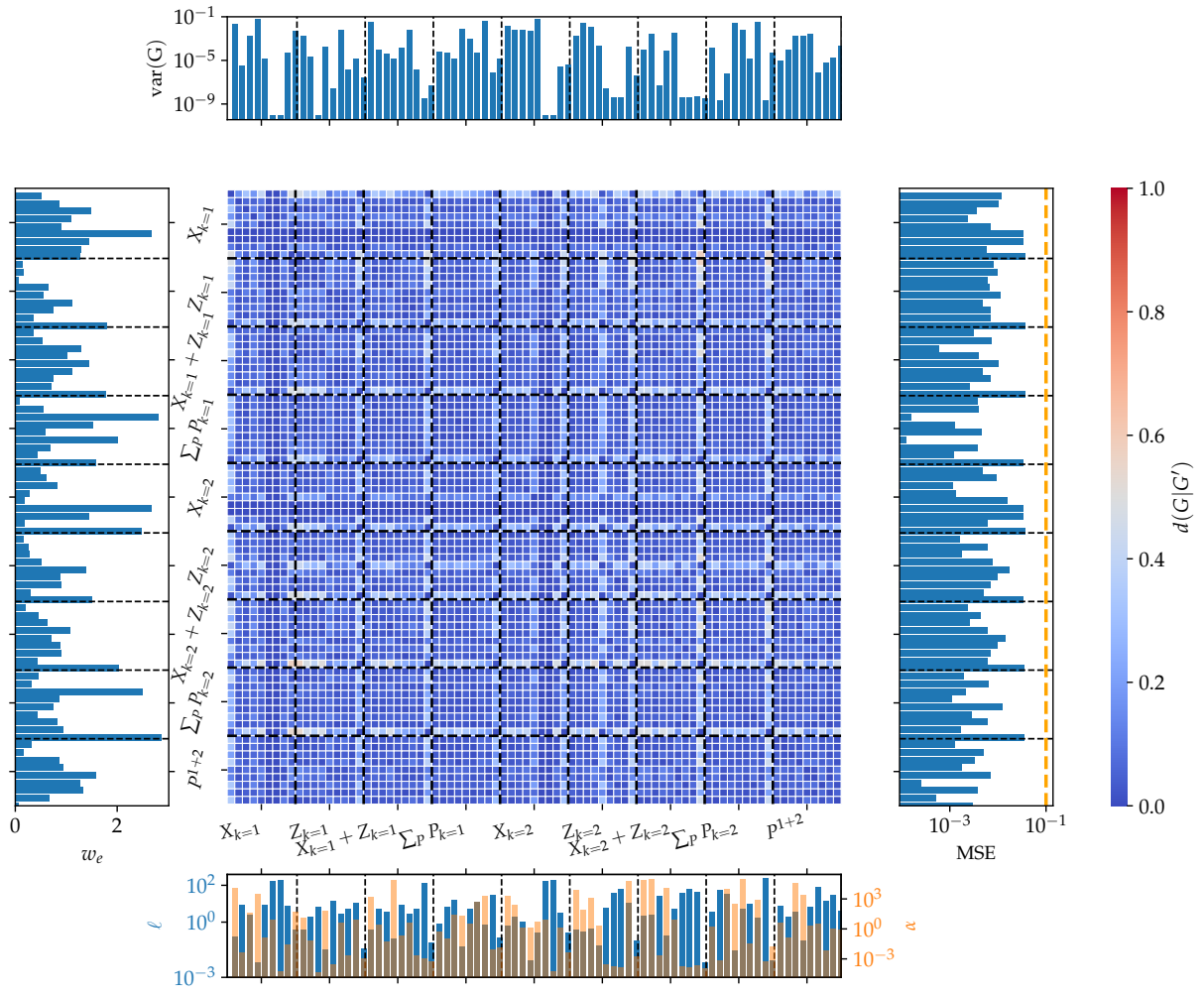


FIG. A22. Analogous illustration to Fig. 12 as discussed in Sec. IV D for the Friedman dataset with $n = 10$ features and the RationalQuadratic outer kernel.

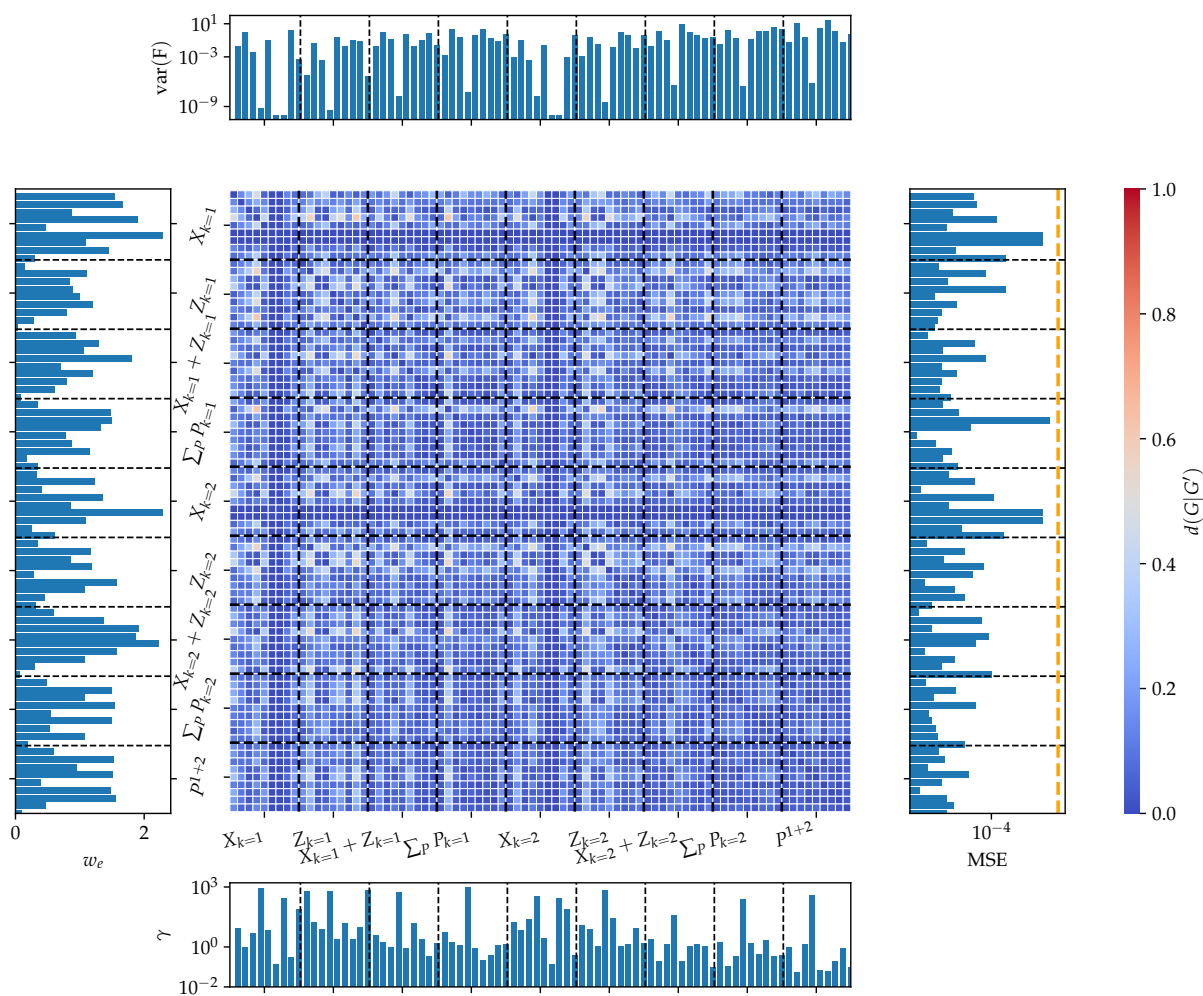


FIG. A23. Analogous illustration to Fig. 12 as discussed in Sec. IV D for the NH_3 -PES dataset and Gaussian outer kernel.

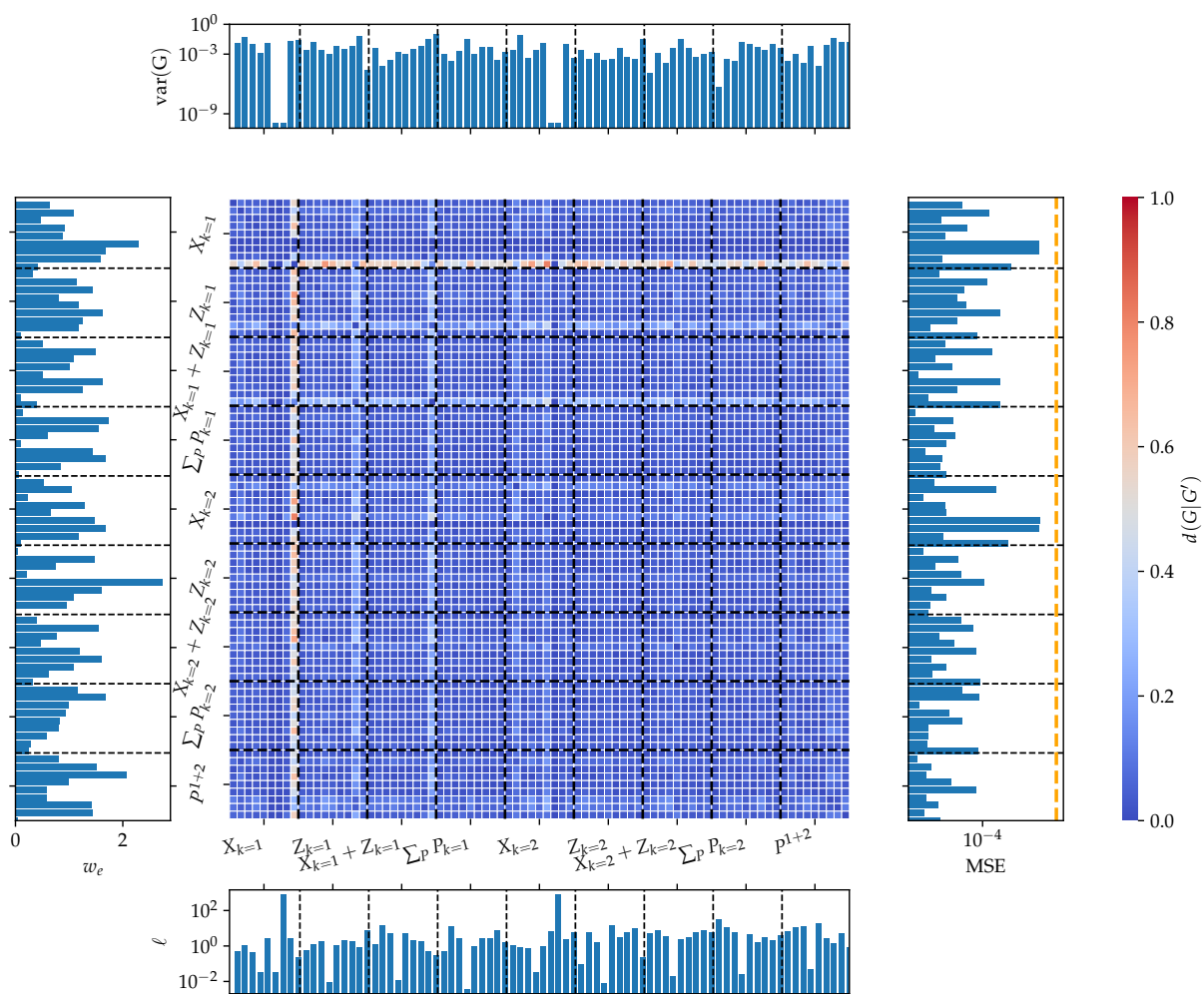


FIG. A24. Analogous illustration to Fig. 12 as discussed in Sec. IVD for the NH₃-PES dataset and the Matérn outer kernel.

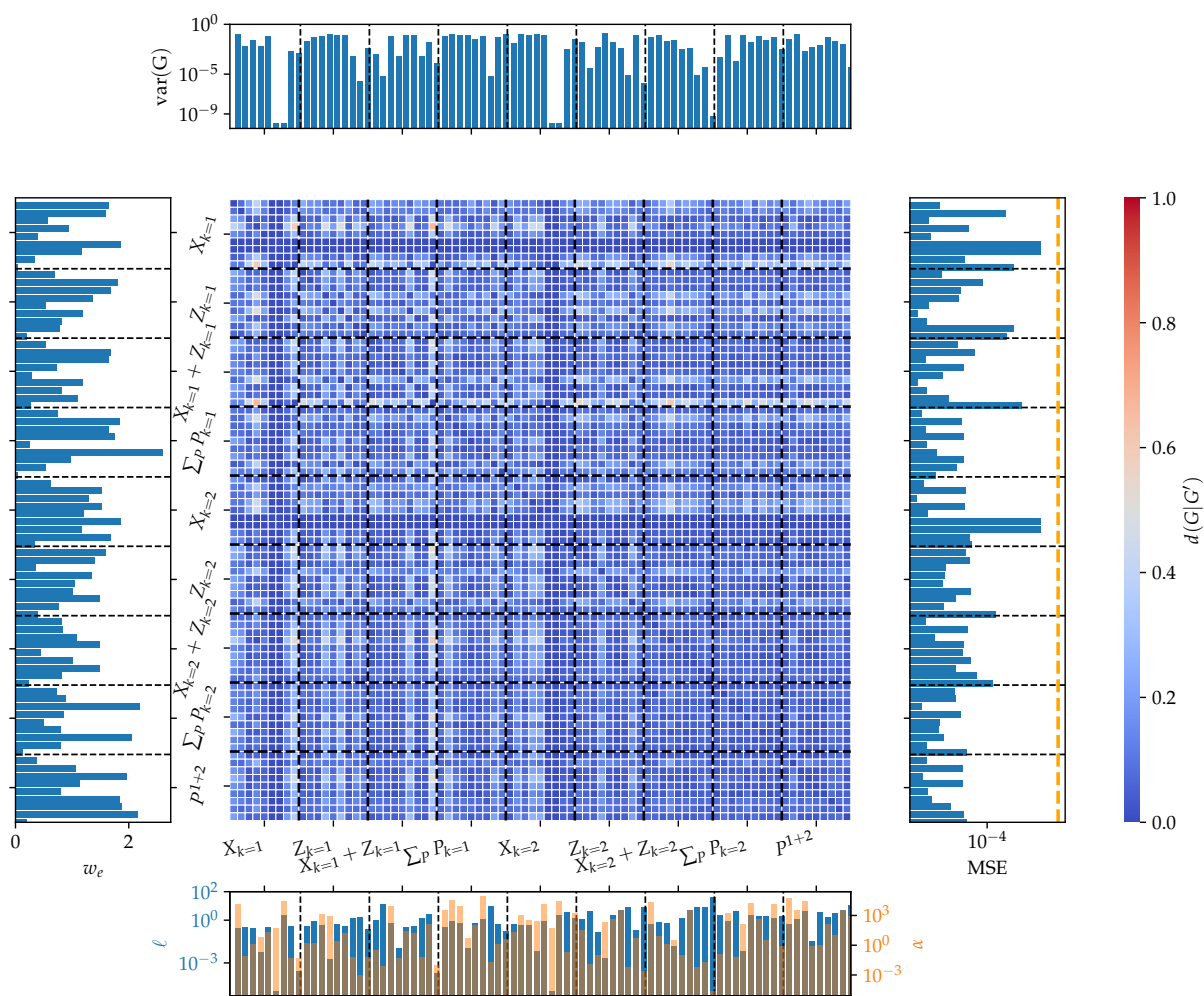


FIG. A25. Analogous illustration to Fig. 12 as discussed in Sec. IV D for the NH₃-PES dataset and the RationalQuadratic outer kernel.

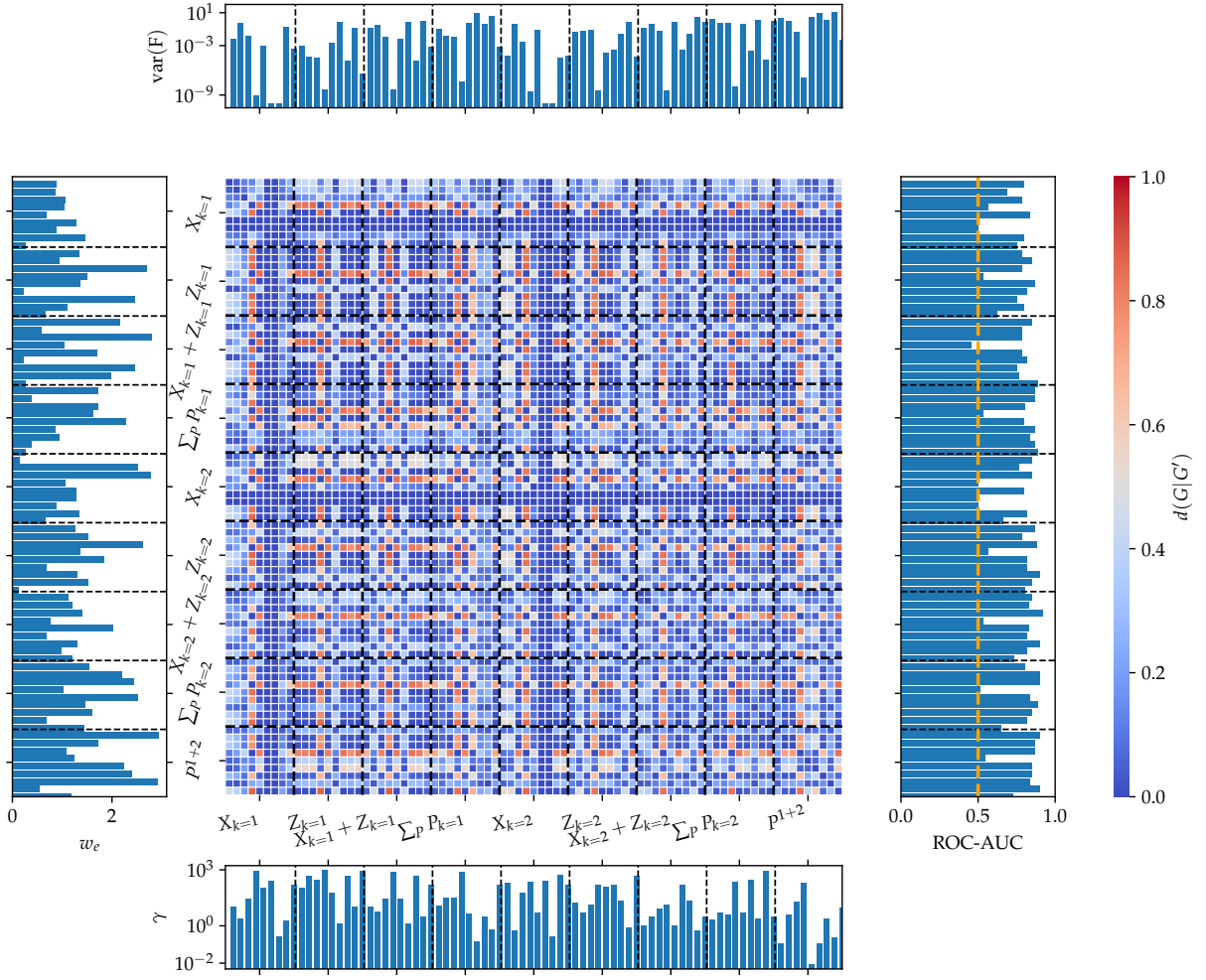


FIG. A26. Analogous illustration to Fig. 12 as discussed in Sec. IV D for the two curves diff dataset with degree $D = 13$ and the Gaussian outer kernel.

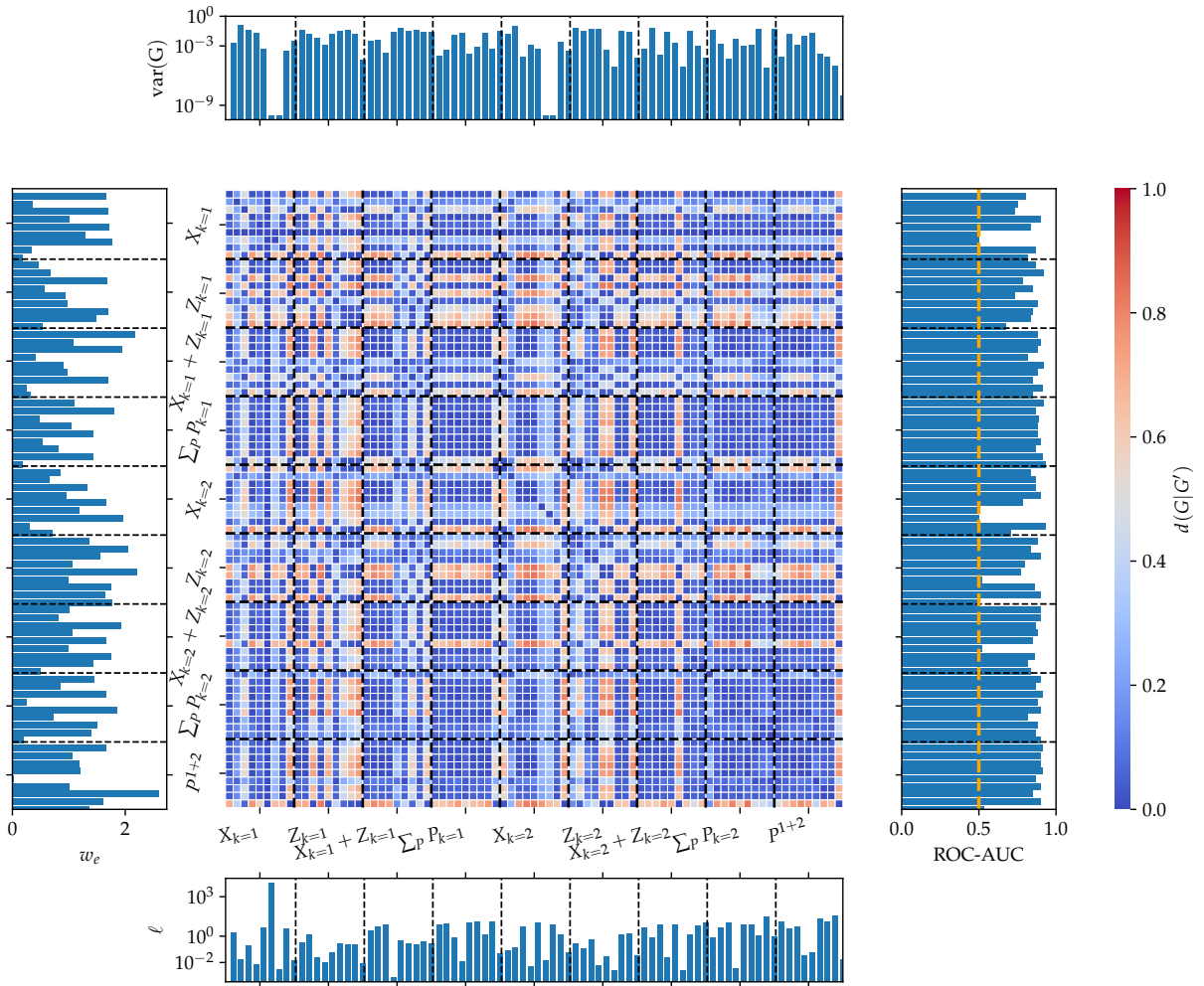


FIG. A27. Analogous illustration to Fig. 12 as discussed in Sec. IV D for the two curves diff dataset with degree $D = 13$ and the Matérn outer kernel.

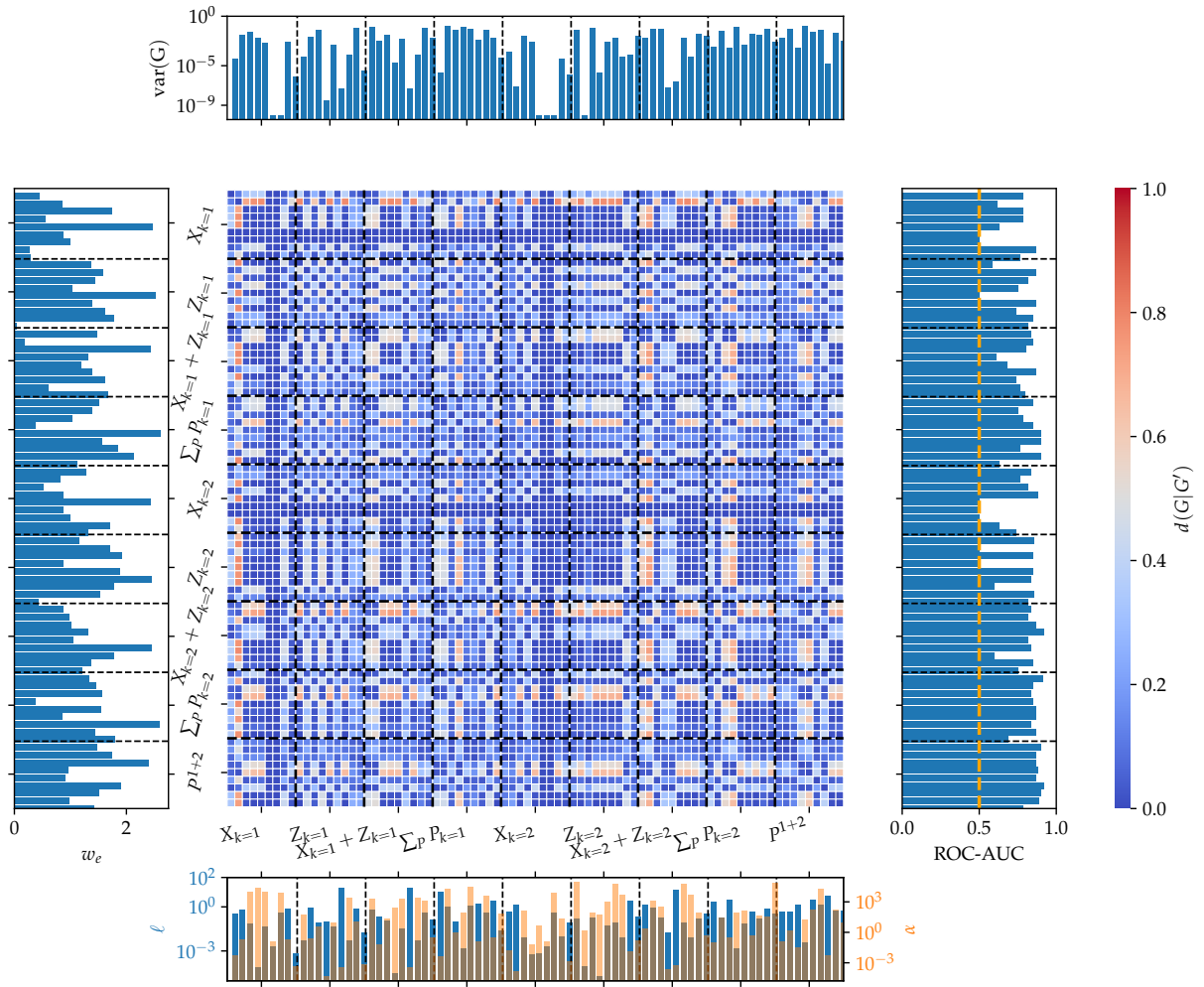


FIG. A28. Analogous illustration to Fig. 12 as discussed in Sec. IVD for the two curves diff dataset with degree $D = 13$ and the RationalQuadratic outer kernel.

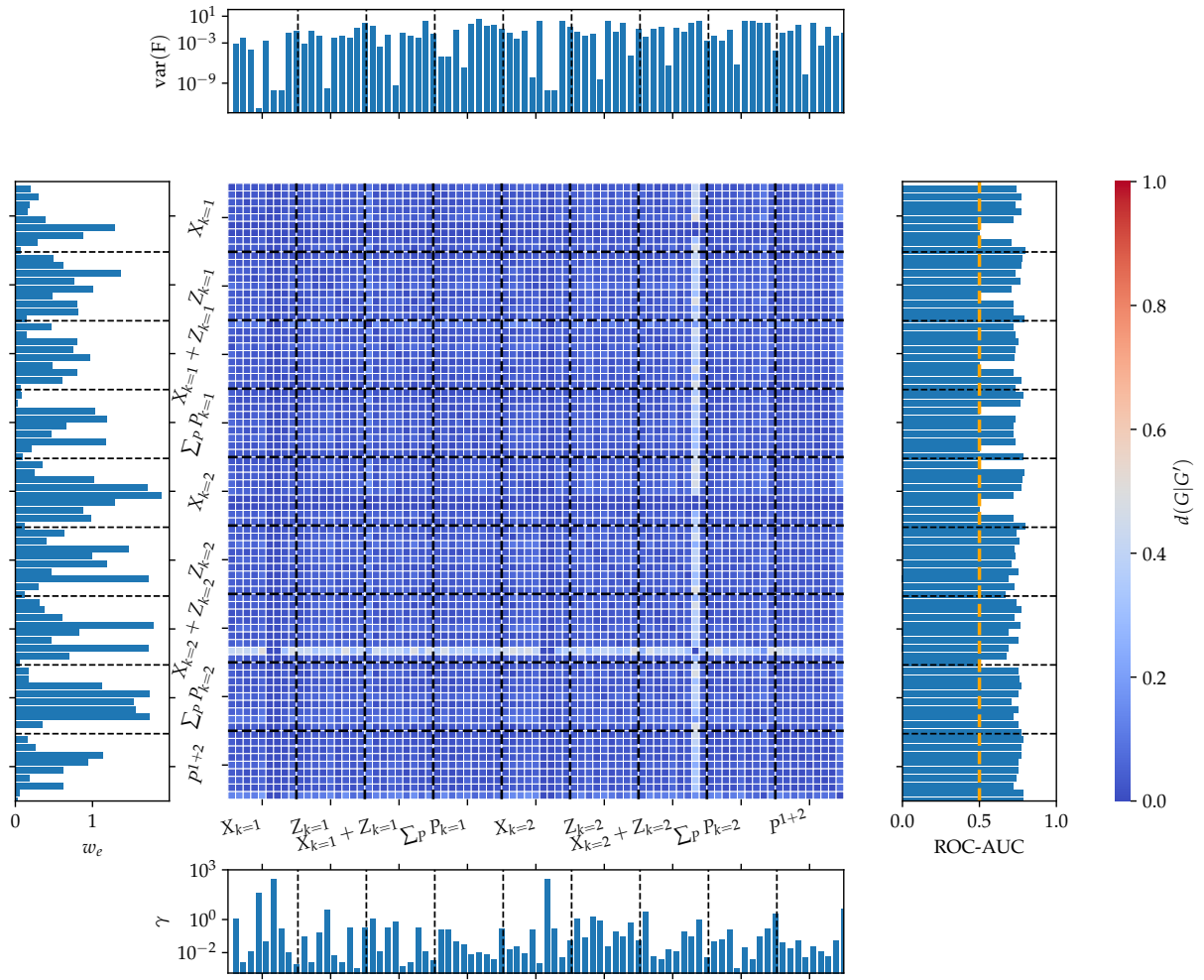


FIG. A29. Analogous illustration to Fig. 12 as discussed in Sec. IV D for the hidden manifold diff dataset with manifold dimension $m = 13$ and Gaussian outer kernel.

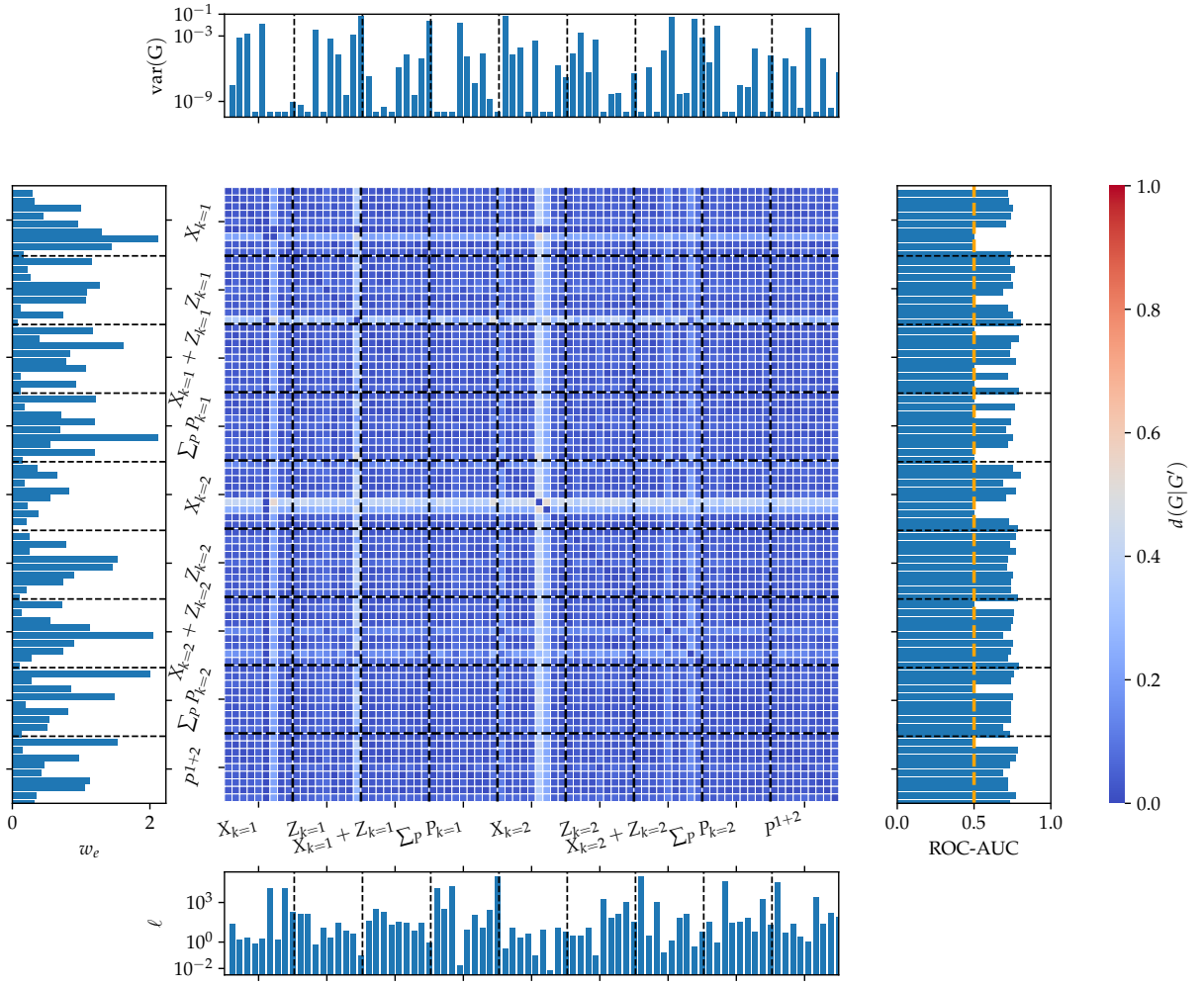


FIG. A30. Analogous illustration to Fig. 12 as discussed in Sec. IVD for the hidden manifold diff dataset with manifold dimension $m = 13$ and Matérn outer kernel.

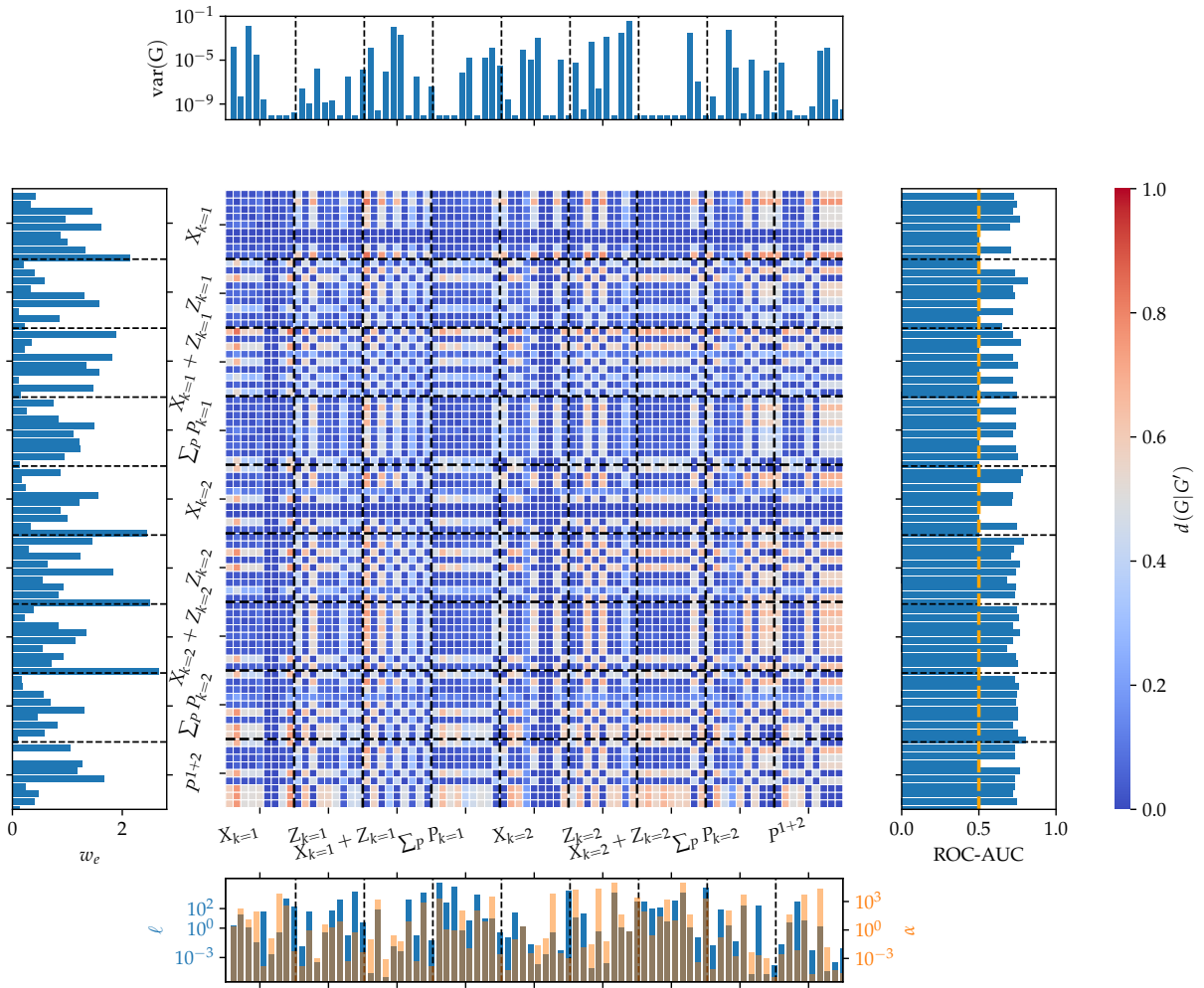


FIG. A31. Analogous illustration to Fig. 12 as discussed in Sec. IVD for the hidden manifold diff dataset with manifold dimension $m = 13$ and RationalQuadratic outer kernel.